Elucidating the microstructure evolution during hydrogen-based direct reduction via a case study of single crystal hematite

Ratzker, Barak; Ruffino, Martina; Shankar, Shiv; Raabe, Dierk; Ma, Yan

Important note
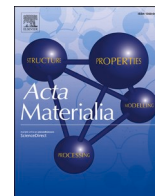To cite this publication, please use the final published version (if applicable).
Please check the document version above.

Full length article

Elucidating the microstructure evolution during hydrogen-based direct reduction via a case study of single crystal hematite

Barak Ratzker [a,1,*] , Martina Ruffino [a,1] , Shiv Shankar [a] , Dierk Raabe [a,*] ,
Yan Ma [a,b,*]

[a] *Max Planck Institute for Sustainable Materials GmbH, Max-Planck-Str. 1, 40237 Düsseldorf, Germany*
[b] *Department of Materials Science and Engineering, Delft University of Technology, Mekelweg 2, 2628 CD Delft, the Netherlands*

ABSTRACT

Sustainable hydrogen-based direct reduction (HyDR) of iron oxide is an effective approach to reduce carbon emissions in steel production. As the reduction behaviour is closely related to the microstructure evolution, it is important to understand the microscopic reduction mechanisms. Industrial hematite pellets are microstructurally intricate systems with inherent porosity, defects, and impurities. Therefore, in the present study we investigated the HyDR of single crystal hematite (at 700 °C) to elucidate the reduction behaviour and microstructure evolution in a model system. The reduction kinetics of the single crystal (SC) were compared to those of industrial polycrystalline porous pellets using thermogravimetric analysis. Additional SC samples were prepared such that their faces are parallel to the (0001), $(10\bar{1}0)$ and $(1\bar{2}10)$ crystallographic planes of hematite, and then partially reduced to 16 and 80 % reduction degree. Their microstructure was thoroughly examined by scanning electron microscopy and electron backscatter diffraction (EBSD). Reaction fronts were thus shown to advance into the hematite by a shrinking core model while creating a percolating pore network in the magnetite layer; this was closely followed by wüstite and iron formation, as well as pore coarsening, with the retained oxides proceeding to reduce homogenously throughout the sample abiding by the pore/grain models. Notably, a "cell-like" morphology develops in the magnetite near the hematite/magnetite interface, with finely porous "cell interiors" surrounded by coarsely porous "cell walls". Furthermore, the hierarchal pore formation, phase transformations, texture, and orientation relationships are considered.

1. Introduction

The goal of reducing anthropogenic carbon emissions necessitates developing more sustainable metallurgical processing pathways for metal production [1]. One of the most promising approaches is the solid-state hydrogen-based direct reduction (HyDR) of iron oxides [2–4]. Substantial efforts have been made to investigate the influence of extrinsic parameters like reducing atmosphere and temperature [2,5] as well as intrinsic factors such as industrial pellet morphologies (e.g., size and porosity) and composition [6,7] on the reduction behaviour and kinetics, to optimise the HyDR process. Meanwhile, it is also critical to gain deeper fundamental understanding of microstructural development during HyDR. The microstructure evolution reflects the underlying reaction mechanisms and plays a vital role in overall kinetics: e.g., affecting both phase and free volume formation/connectivity, as well as

mass transport, phase nucleation, micromechanics/deformation and fracture, and water vapour confinement [8–10]. Improved understanding of these fundamental microstructural aspects can then be leveraged for large-scale process and pellet design, to realise efficient reactor concepts that achieve high metallisation degrees as quickly as possible at reduced energy costs, to help accelerating the decarbonisation of the global steel sector.

Industrial pellets used in iron production are sintered polycrystalline aggregates of porous iron oxide particles. They play a complex and multifaceted role in green steel making: they provide the iron feedstock with lowest possible gangue content, carry huge mechanical loads inside the reactor, must have low abrasion to avoid sticking and unwanted particle baking, and they must ensure gas percolation and temperature balancing in the counter-flow reactor, thus altogether helping to increase reduction process efficiency. However, the complexity of their

---

* Corresponding authors.
  E-mail addresses: b.ratzker@mpie.de (B. Ratzker), d.raabe@mpie.de (D. Raabe), y.m.ma@tudelft.nl (Y. Ma).
[1] Equal contribution.

microstructure, inherited sinter pore structure and chemistry make the fundamental understanding of the microstructure evolution during HyDR very challenging [11], such that up to date it has been difficult to disentangle the relationships between structure, property and transport in these materials, irrespective of their eminent role in the coming green steel revolution.

In contrast, high-purity iron oxide single crystals (SC), which exclude factors like inherited sinter porosity, crystal defects, interfaces, and gangue elements, can serve as model systems to investigate the microstructural evolution during the HyDR process – eliminating the shortcomings associated with pellet characterization. In the literature, most studies performed on SCs focused on the reduction of hematite to magnetite in a reducing CO atmosphere [12–21]. In contrast, only a few studies have been carried out on the HyDR of hematite [5,14] or magnetite [22] SCs.

Previous studies on the direct reduction of SC or dense sintered hematite showed that the morphology of the magnetite product varies depending on reduction temperature. At low temperatures (≤650 °C), a cellular magnetite reaction front was observed with uniform, fine and regularly-spaced nanopore channels, while dense lamellar or plate-like magnetite formed at higher temperatures (≥800 °C) [12,15]. At intermediate temperatures, a mixed morphology was found in the magnetite [12,23]. Additionally, the oxygen partial pressure was shown to play a role in modifying the magnetite morphology (cellular or lamellar),

altering to some extent the temperatures at which the different morphologies of magnetite were observed [15,20].

In general, the direct reduction of iron oxides follows a topochemical pathway, i.e. reduction occurs at distinct interfaces between solid phases, which remain parallel to the exterior surface of the initial oxides as they move inward [24,25]. The reduction process of polycrystalline iron oxide pellets has often been described by either a shrinking core model [26,27], in which a reaction front moves inward, forming a reduced shell around an unreacted core, or by a pore/grain model [12,28], in which reduction occurs uniformly throughout the whole porous structure without macroscopic gradients. Bitsianes and Joseph [24] studied the microstructures of various types of dense hematite (i.e., SCs, natural ore, and sintered bodies) that were partially reduced (~25–35 %) by hydrogen at 600–900 °C, showing that the topochemical process generally developed shrinking core behaviour at the macroscopic scale.

Nevertheless, most of the previous studies on the direct reduction of hematite SCs have been limited to the hematite to magnetite transformation. To the best of our knowledge, none have involved a comprehensive investigation of the entire direct reduction process from SC hematite to metallic iron. Particularly, the correlation between microstructural features in the sequential reduction steps remains unclear, with regards to the phase transformations and induced porosity in a dense SC as well as their crystallographic dependence.

In the present study, we therefore systematically investigate the
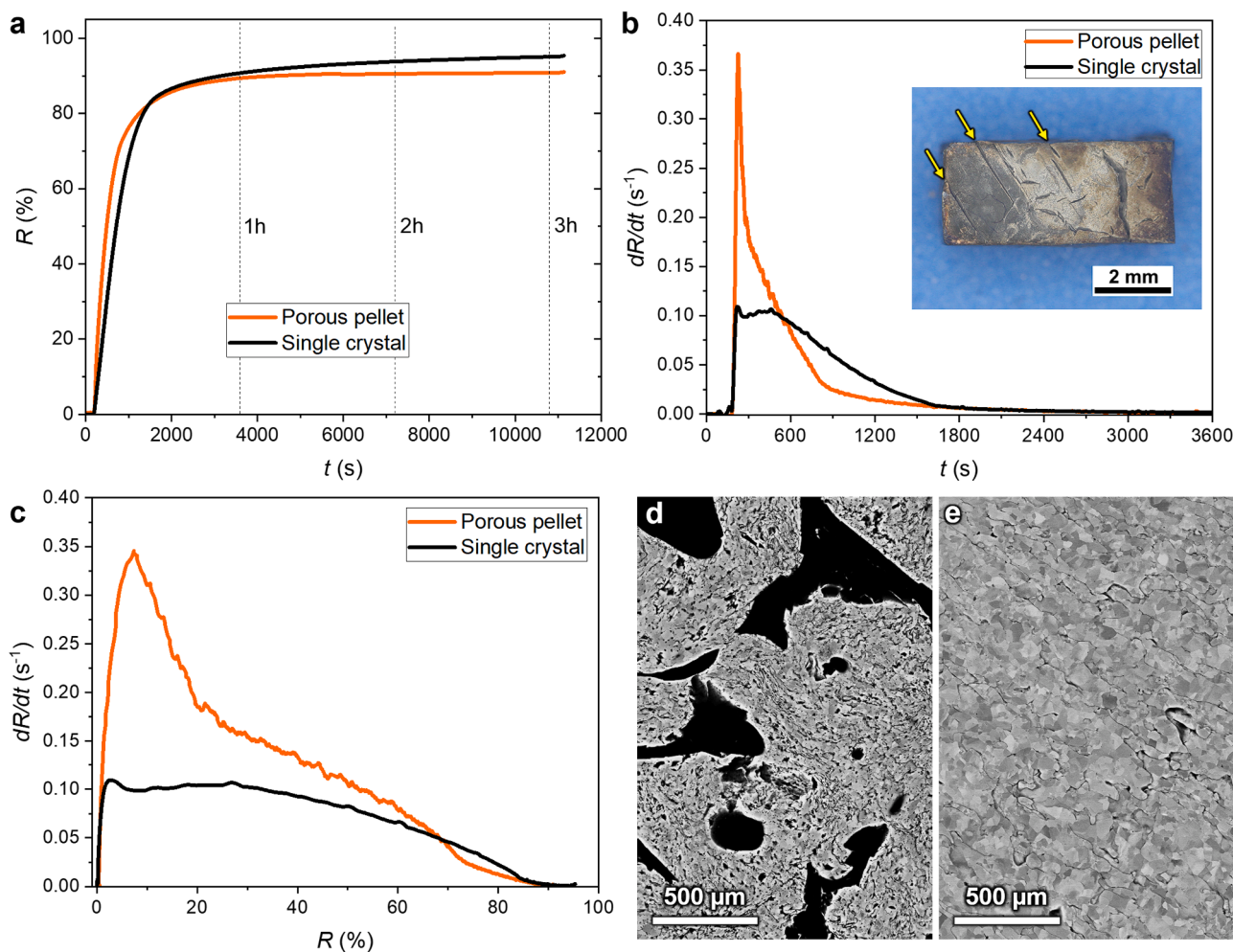
Fig. 1. Reduction kinetics of a dense single crystal (SC) hematite sample and a porous pellet sample (~30 % inherited porosity from sintering prior to onset of reduction) reduced isothermally at 700 °C in pure hydrogen for 3 h. (a) Reduction degree (R) as a function of time (t), (b) reduction rate (dR/dt) as a function of time, a photograph of the reduced SC is inserted (directional cracks that formed during reduction are indicated by arrows), and (c) reduction rate as a function of reduction degree. SEM micrographs showing the microstructure of the 3 h-reduced (d) porous pellet and (e) SC samples.

HyDR behaviour of SC hematite with pure H_2 at an intermediate temperature of 700 °C, focusing on analysing the microstructure evolution, including the phase distribution and morphology of pores for different crystallographic crystal facets, at the early and advanced stages of reduction, i.e. at 16 % and 80 % partial reduction. This approach enables us to elucidate the porosity development and microscale reduction sequence of Fe_2O_3 (hematite, corundum structure with hcp oxygen sublattice) → Fe_3O_4 (magnetite, inverse spinel structure with fcc oxygen sublattice) → $Fe_{1-x}O$ (wüstite, halite structure with fcc oxygen sublattice) →α-Fe (bcc structure) using as starting surfaces three different crystallographic planes of hematite.

2. Experimental

2.1. Hydrogen-based direct reduction experiments

A slab of pure hematite SC with dimensions of 7 mm × 7 mm × 2 mm (MaTecK GmbH) was used in this study. Several rectangular samples (3 mm × 3 mm × 2 mm) were cut from the SC using a diamond wire saw for interrupted reduction experiments. In each sample, the base of the slab was oriented along the basal plane (0001) of hematite, while the two lateral faces of the slab were parallel to the $(10\bar{1}0)_{hem}$ and $(1\bar{2}10)_{hem}$ planes – as shown in the supplementary information (SI) (Figure S1a,b). Each slab weighed roughly 0.1 g. To assess the overall reduction kinetics of SC hematite, one additional sample was prepared by cutting a SC into a ~6 mm × 3 mm × 2 mm slab, weighing roughly 0.2 g. For comparison, a porous polycrystalline sample was also prepared by cutting a pre-dried industrial hematite pellet (with ~30 % porosity inherited from the prior sintering manufacturing process, similarly to the porosity in the pellet studied in [8]) into a 5 mm × 5 mm × 5 mm cube, weighing roughly 0.35 g.

Hydrogen-based direct reduction of the samples was carried out in an in-house thermogravimetric analysis (TGA) setup in a vertical quartz tube furnace [29]. Temperature-programmed experiments were conducted according to the following protocol, with the temperature being measured and controlled by a thermocouple inserted into the centre of a reference pellet. For each reduction experiment, a sample was laid on a 304 stainless steel mesh inside an open quartz basket connected to a precision balance (0.1 μg resolution). The sample was placed such that the base of the slab was oriented along the basal plane of the SC (Figure S1c) and exposed to pure hydrogen (99.999 % purity) at a flow rate of 10 L/h. Then, the sample was heated rapidly to 700 °C by infrared light with a ramping rate of 5 °C/s and held isothermally for 3 h for the kinetic analysis. Additional SC samples were partially reduced by exposing them to hydrogen at 700 °C for 2.5, 4, and 15 min for microstructure analysis at intermediate reduction stages, corresponding to a reduction degree of 16, 27, and 80 %, respectively. At the end of the isothermal process, the infrared light was switched off and the samples were cooled down to room temperature. During the experiments, the mass change of each sample was continuously monitored by the balance. The total reduction degree was determined from the measured mass loss divided by the theoretical mass loss, considering Fe_2O_3 being fully reduced into Fe.

2.2. Microstructure characterization

The reduced SC samples were cut by a diamond wire saw to expose different projection directions for each crystallographic plane facet. Metallographic preparation of the samples included mounting in a conductive resin and grinding with SiC abrasive papers followed by polishing using diamond microparticle and silica nanoparticle suspensions. For the partially reduced samples both cross-sectional and ground-in surfaces were prepared, such that the microstructure could be observed in projection perpendicular or parallel to the reduction front for the different crystal facets. The microstructures were examined using

a Zeiss Merlin high-resolution scanning electron microscope (SEM) by backscattered electrons (BSE) and electron channelling contrast imaging (ECCI) [30], operated at 10 kV and 2.2 nA. Electron backscatter diffraction (EBSD) maps were collected using an EDAX DigiView 5 camera and EDAX APEX software. The Kikuchi pattern data sets were analysed by spherical indexing using EDAX OIM Matrix v.9 software [31].

3. Results

3.1. Reduction kinetics of single crystals vs. polycrystalline porous pellet

The isothermal reduction kinetics of a dense SC hematite sample were assessed in comparison to a porous polycrystalline hematite sample prepared from an industrial pellet. The reduction degree (*R*) and reduction rate (*dR/dt*) as a function of time (*t*) as well as the reduction rate as a function of reduction degree are presented in Fig. 1. The SC sample reduced more slowly than the pellet sample: during the first 6 min of isothermal holding at 700 °C, the reduction rate of the pellet was roughly 2 times faster than that of the SC sample. During that period of time, the pellet reached a reduction degree of 55 %, while the SC sample was reduced by only 35 % (Fig. 1a,b). The reduction rate of the pellet sample remained faster than that of the SC sample up to a reduction degree of ~70 %, after which the reduction rate of the pellet dropped below that of the SC (Fig. 1c). At the final reduction stage (above 85 % reduction degree) both samples exhibited extremely sluggish reduction rates of <0.001 s⁻¹ (Fig. 1c). Note that both samples did not reach 100 % conversion into iron due to sintering and the trapping of oxide by dense metallic iron (Figure S2). The SC and pellet samples reached a reduction degree of 96 and 91 %, respectively. The lower reduction degree of the pellet is attributable to the presence of additional gangue oxides (e.g., SiO_2, Al_2O_3, CaO, MgO) in the industrial pellet (~93.7 iron oxide purity declared by the manufacturer, with ~4.2 % of that being magnetite). The faster reduction kinetics of the pellet can be attributed to its initial porous structure, which provides a percolating network for gas transport throughout the sample and free surfaces for the chemical reactions (i.e. the removal of oxygen with hydrogen). Nevertheless, despite the lack of any initial porosity in the SC, the sample still reduced at a reasonable rate (91 % after 1 h holding at 700 °C), and only the final few percent were very sluggish (<0.002 s⁻¹) – reaching 96 % after an additional 2 h (Fig. 1a).

Observing the reduction rate as a function of time and reduction rate as a function of the time-dependent reduction percentage (Fig. 1b,c) provides insight into the progression of the reduction process. The pellet sample displays typical discernible sequential acceleration and deceleration stages that reflect the changes in the reduction rates of different iron oxide phases [8,11]. It can be seen that the process started with rapid Fe_2O_3→Fe_3O_4 reduction in the first 2 min (reaching up to ~0.36 s⁻¹), followed by slower Fe_3O_4→$Fe_{1-x}O$ (wüstite, where x indicates a deficiency of iron cation ions from stoichiometry) and finally the slowest $Fe_{1-x}O$→Fe stage. The trend is different for the SC: initially the reduction rate increased at a rate similar to that of the pellet sample but plateaued (at ~0.1 s⁻¹) after ~1 min, remaining so until about 30 % reduction (Fig. 1c). The reduction rate then started to decrease roughly monotonously and finally became sluggish over the last ~10 %.

The microstructure of the reduced pellet sample (for 3 h) exhibits a typical direct reduced porous iron microstructure [8] with an inherited macroscopic pore network and acquired micro- and nanoscale pores (Fig. 1d). The reduced SC displays some visible cracks that formed during the reduction process, most of which appear to follow a preferential crystallographic orientation (Fig. 1b insert). These cracks created additional free surfaces for chemical reactions ($O+H_2→H_2O$) in the SC sample. In contrast to the porous reduced pellet sample, the reduced SC is mostly dense (besides the highly porous regions near free surfaces, see Figure S3), mainly displaying only residual submicron/nano pore networks with ~1–3 % acquired porosity (Figures 1e and S3e,f). Note that
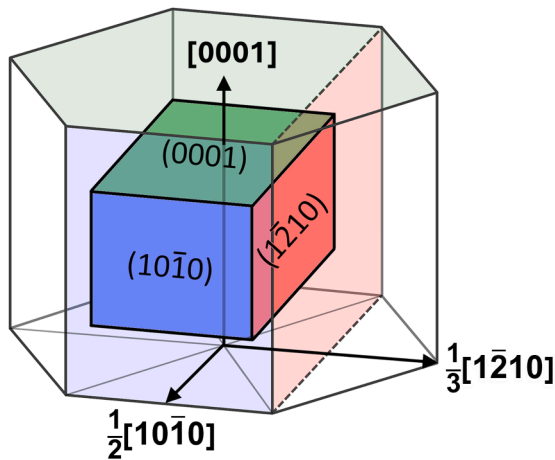
Fig. 2. Schematic of the relationship between the orientation of the SC samples (cube) and the conventional unit cell of hematite (hexagonal prism). Crystallographic planes of hematite and the relative projection directions are marked.

the direct reduced iron derived from the SC also appears to have a larger average grain size (~1.5 μm) compared with the reduced pellet sample (~0.8 μm). Additional higher magnification micrographs of the reduced samples' microstructure are provided in SI Figures S2 and S3.

3.2. Microstructure evolution in partially reduced single crystals

For ease of interpretation of the studied SC orientations and projection directions in the micrographs to follow, in Fig. 2 we provide a schematic relating the orientation of the SC samples (represented as a cube) to the conventional unit cell of hematite (represented as a hexagonal prism). The faces of the SC cube are parallel to principal crystallographic planes of hematite, namely $(0001)_{hem}$, $(10\bar{1}0)_{hem}$ and $(1\bar{2}10)_{hem}$.

Fig. 3 shows an overview of the partially reduced SC samples with reduction degrees of 16 % and 80 %, after isothermal holding at 700 °C for 2.5 and 15 min, respectively. The SC samples were sectioned parallel to the three principal crystallographic planes highlighted in Fig. 2, such that Fig. 3 displays the SEM micrographs of the cross-sections in projection along $[10\bar{1}0]_{hem}$, $[1\bar{2}10]_{hem}$, and $[0001]_{hem}$. The 16 %-reduced sample displays a topochemical shrinking core reduction behaviour, as suggested by the reduced frame surrounding the unaffected hematite core. The reduced frame presents small but noticeable variations in thickness across the different crystallographic plane facets: the average thickness of reduced layers originating from both $(0001)_{hem}$ basal plane facets is ~150 μm, while the layers originating from the $(10\bar{1}0)_{hem}$ and $(1\bar{2}10)_{hem}$ plane facets are ~130 μm thick. The cracks in the hematite nucleated and propagated parallel to the reaction front during the rapid cooling after the interrupted reduction due to differences in thermal expansion coefficients (~18 % difference between hematite and magnetite at 700 °C [32]). As the reduction progressed to a higher reduction degree of 80 %, the macroscale core-shell feature was lost. Instead, the 80 %-reduced sample displays a generally homogeneous microstructure and reduction behaviour at the sample scale, with evident reduction fronts converging towards the centre. Moreover, the sample is slightly misshapen with rounded corners and contains large diagonal cracks, as also seen macroscopically in the fully reduced sample (Fig. 1b insert).

Several other features can be observed upon closer inspection of the reduced layers, as shown in the backscattered electron (BSE) micrographs in Fig. 4. At these magnifications, it is apparent that the white phase is iron, the bright grey is magnetite/wüstite, and the darker grey is hematite. There is a discernible interface between reduction fronts propagating from two perpendicular surfaces, starting at the corner and continuing diagonally towards the centre of the samples observed in both partially reduced samples (Fig. 4d,e). The angle between the interface and the $(10\bar{1}0)_{hem}$ or $(1\bar{2}10)_{hem}$ facets is roughly 40° (see Fig. 3d and 4d), confirming that the reaction front advanced more quickly in the direction perpendicular to the basal planes compared to
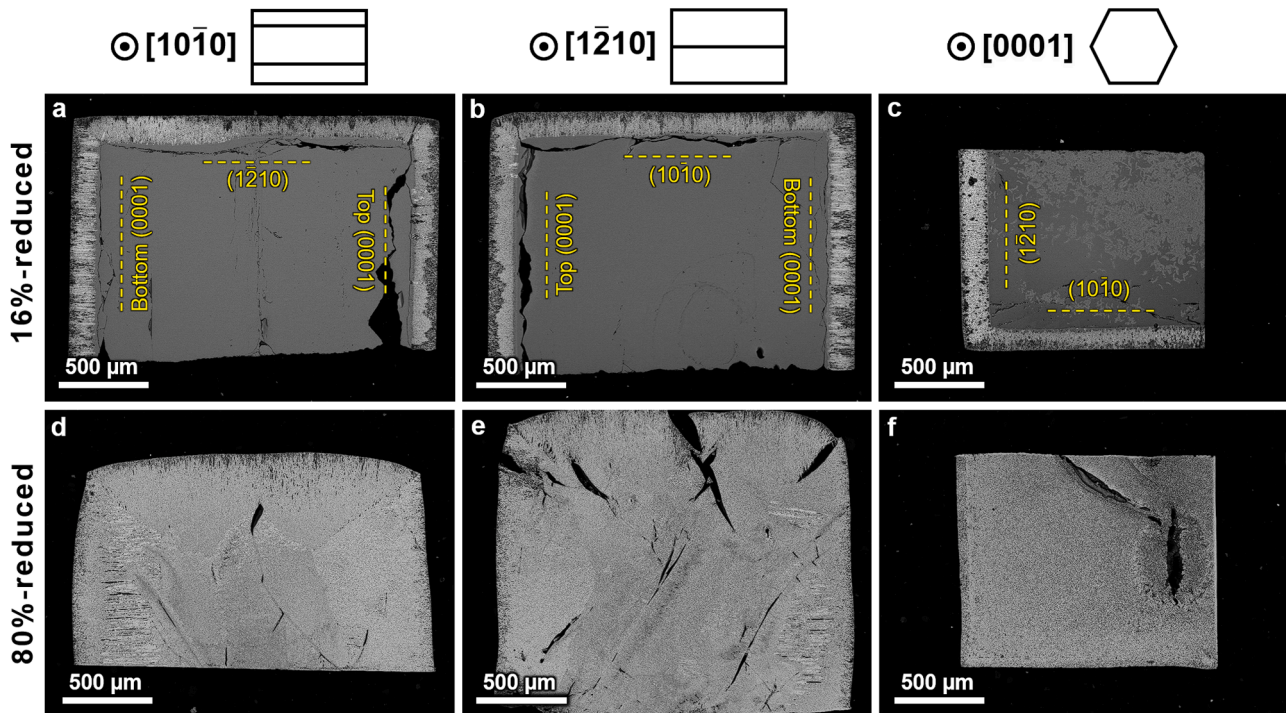
Fig. 3. SEM-BSE micrographs of cross-sections of the partially reduced samples with (a)-(c) 16 % and (d)-(f) 80 % reduction degree. (a) and (d) cross-sections viewed in projection along the $[10\bar{1}0]_{hem}$ direction, (b) and (e) cross-sections viewed along the $[1\bar{2}10]_{hem}$ direction, (c) and (f) cross-sections viewed along the $[0001]_{hem}$ direction.
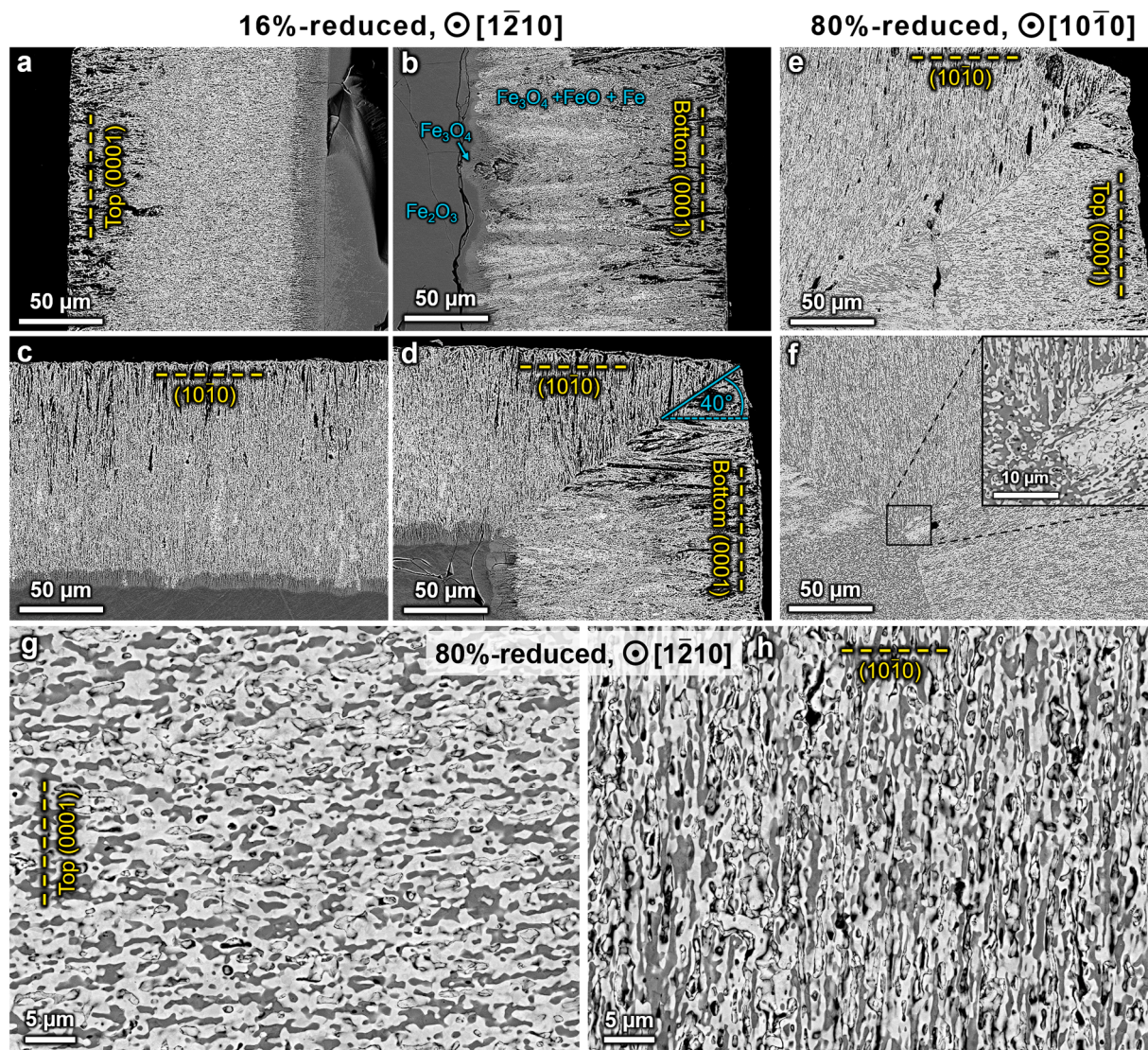
Fig. 4. SEM-BSE micrographs of cross-sections of partially reduced samples. 16 %-reduced sample in projection along $[1\bar{2}10]_{hem}$: (a) top and (b) bottom basal plane facets, (c) $(10\bar{1}0)_{hem}$ plane facet, and (d) the corner between the $(10\bar{1}0)_{hem}$ and bottom $(0001)_{hem}$ facets. 80 %-reduced sample: (e) corner and (f) inner region showcasing a triple point of converging reduction fronts from different crystallographic plane facets, in projection along $[10\bar{1}0]_{hem}$; higher-magnification micrographs of the (g) top basal and (h) $(10\bar{1}0)_{hem}$ plane facets in projection along $[1\bar{2}10]_{hem}$.

the other crystallographic plane facets. The 80 %-reduced sample further reveals that the mixture of iron and oxide persists uniformly throughout the reduced layer for each plane facet (Fig. 4e–h). Directionality of the pores and partitioned phases is evidently a vestige of the topochemical reduction behaviour, as the flux of Fe ions is directed away from the surface of the crystal and into the bulk. Fig. 4 g,h shows higher-magnification micrographs of iron-rich regions in the reduced layers originating from the top basal plane and $(10\bar{1}0)_{hem}$ plane facets, in projection along $[1\bar{2}10]_{hem}$. Through image analysis of these regions, it can be determined that the reduced layer of the top basal plane contains a higher ratio of metallic iron to residual oxides (64 % iron and 36 % oxide) than that of the $(10\bar{1}0)_{hem}$ plane (61 % iron and 39 % oxide). Moreover, the top basal plane reduced layer contains only 3 % porosity, as opposed to 11 % in the $(10\bar{1}0)_{hem}$ facet reduced layer.

In addition, there is a noticeable difference in the microstructure of the reduced layers between the two facets oriented along the $(0001)_{hem}$ basal plane – observed as the sides of the sample when viewed in projection along $[10\bar{1}0]_{hem}$ or $[1\bar{2}10]_{hem}$ in Figs. 3 and 4. One basal plane facet (originally the top surface in the TGA setup, see Figure S1) presents

a uniform microstructure (Fig. 4a), similar to that of the other two $(10\bar{1}0)_{hem}$ or $(1\bar{2}10)_{hem}$ facets (Fig. 4c). In contrast, the second basal plane facet (originally the bottom surface in the TGA setup) is distinctly different (Fig. 4b). The microstructure of the reduced layer originating from the bottom $(0001)_{hem}$ basal plane facet contains continuous streaks of iron with abundant oxide in between and larger elongated pores perpendicular to the basal plane (Figs. 3a,d and 4c), whereas the top $(0001)_{hem}$, $(10\bar{1}0)_{hem}$ and $(1\bar{2}10)_{hem}$ plane facets display a more homogenous mixture of oxides and metallic iron (Fig. 4a,c). However, it should be noted that sporadic Fe-dense protrusions can occasionally be found in the reduced layer of the top basal plane facet (Figure S4a,b). Furthermore, the hematite/magnetite interface parallel to the bottom basal plane (Fig. 4b) is considerably more jagged compared to the interfaces parallel to all other crystallographic planes examined (Fig. 4a, c). The same streaking morphology in the reduced bottom basal plane facet is also clearly observed in the 80 %-reduced sample (Figure S4c). We suppose that the peculiarity of the different microstructural morphology in the reduced bottom basal plane facet originated from the different gas flow conditions developed at the bottom of the sample. As in the vertical TGA system gas flows from the bottom to the top of the
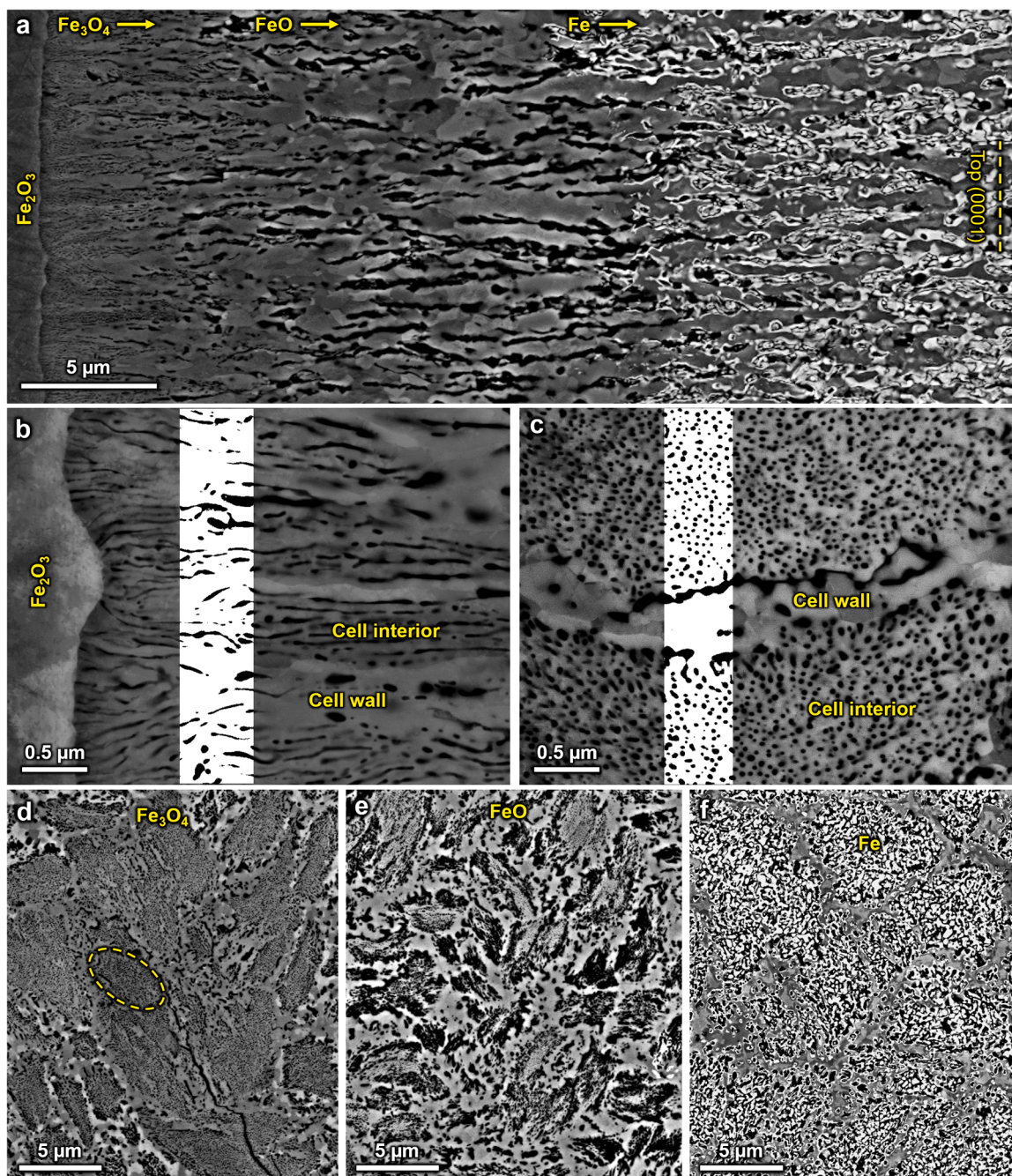
Fig. 5. SEM-BSE micrographs of different regions in the 16 %-reduced sample imaged perpendicular and parallel to the reduction front. (a) Reduced layer originating from the top basal plane facet viewed along the $[1\bar{2}10]_{hem}$ direction, showing the hierarchical change in porosity from the hematite/magnetite interface into the region where metallic iron formed. The wüstite is discernible as a brighter grey than the magnetite. Higher magnification micrographs of the reduced region in the vicinity of the migrating magnetite/hematite interface as viewed along the (b) $[1\bar{2}10]_{hem}$ and (c) $[0001]_{hem}$ directions. The white overlays shown in (b) and (c) exemplify converted binary images for porosity analysis (see Discussion section 4.2). Representative micrographs of the reduced regions at different depths from the bottom basal plane facet surface viewed along the $[0001]_{hem}$ direction containing predominantly (d) magnetite, (e) wüstite, and (f) iron.

tube, turbulence and faster gas exchange possibly occurred at the bottom of the SC sample that was laid flat against the basket (see the schematic drawing in Figure S1).

Studying the reduced layer at high magnifications reveals the hierarchical morphology of developed porosity, as shown in Fig. 5. Pores nucleate at the hematite/magnetite interface by accumulation of vacancies and form elongated nanoscale channels left behind the migrating reaction interface (Fig. 5b). The pore morphology was further elucidated by imaging the reduced interfaces in the projection of the plane facet, for example, the $(0001)_{hem}$ basal plane facet along the

$[0001]_{hem}$ direction (Fig. 5c). This was accomplished by grinding down the reduced layer of the facet, allowing to image the reduced layer at a depth of ~150 μm from the original surface. From this perspective, an evident cell-like structure is observed in the magnetite, comprising regions with densely packed nanopores (i.e. the "cell interiors") enclosed by dense "cell walls" containing coarser submicron-sized pores (Fig. 5c–e). This cell morphology formed in the magnetite close to the hematite interface for all crystallographic plane facets. However, the size and shape of the cells, as well as thickness of the walls, varies depending on the plane facet (Figure S5). The cells are relatively small
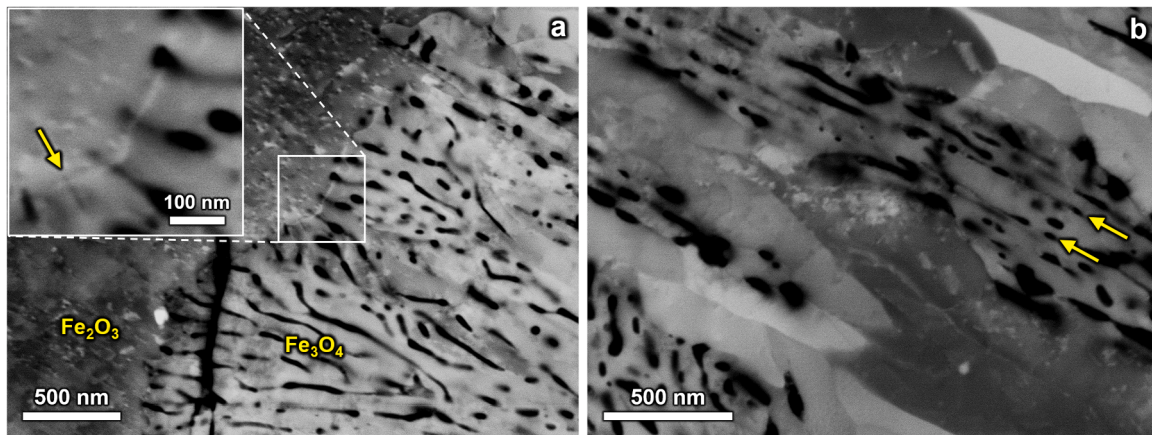
Fig. 6. Electron channelling contrast imaging (ECCI) micrographs of the 16 %-reduced bottom basal plane magnetite regions along projection direction of $[1\bar{2}10]_{hem}$ taken at the (a) hematite/magnetite interface and (b) the reduced region in the vicinity of the interface; examples of straight nanopore channels nucleation sites are marked with yellow arrows in (a) and (b). Defects are enhanced scattering sites and appear bright in the dark electron channelling contrast.

($\sim$1–2 μm wide) in the reduced layers of the $(10\bar{1}0)_{hem}$ and $(1\bar{2}10)_{hem}$ plane facets (observed in projection along $[10\bar{1}0]_{hem}$ and $[1\bar{2}10]_{hem}$, respectively), larger ($\sim$1.5–3 μm wide) in the top basal plane facet and considerably larger ($\sim$2–5 μm wide) in the bottom basal plane facet. Note that the cell wall thickness varies proportionally to the cell size (Figure S5). Furthermore, in the $(10\bar{1}0)_{hem}$ and $(1\bar{2}10)_{hem}$ plane facets the cells are roughly equiaxed, while in the top and bottom $(0001)_{hem}$ basal plane facets they are mostly oval with the major axis diameter being roughly $\sim$2–3 times longer than the minor axis (Figs. 7a–c and 8a-c).

Additional microstructural features in the magnetite product near the hematite interface were revealed by ECCI [30] of the bottom basal plane in projection along the $[1\bar{2}10]_{hem}$ (Fig. 6). First, a high density of slip dislocations is observed in the hematite in the vicinity of the hematite/magnetite interface. Given that the dislocation lines are visible in the $[1\bar{2}10]_{hem}$ projection, these dislocations are thought to accomplish basal slip. As the critical resolved shear stress in hematite at 700 °C is only $\sim$40 MPa [33], the activation of this slip system is feasible, possibly to accommodate stresses induced by the large volume mismatch between the different phases. Secondly, the bright contrast suggests that there is an accumulation of defects at the hematite/magnetite interface (Fig. 6a insert). It should be noted that although some pores are perceived to be inside hematite, it only appears that way due to the interface being inclined to the observation surface (so that pores within magnetite below the surface are detected). Some straight nanopore channels ($\sim$5–35 nm in diameter) appear to have served as the initial stage of pore nucleation (marked by arrows in Fig. 6). These channels are observed at the hematite/magnetite interface (Fig. 6a insert) and extend several microns into the magnetite leading away from the hematite/magnetite interface, with larger pores nucleating along them (Fig. 6b). In addition, there are various grains, subgrains, and dislocations within the dense magnetite regions (Fig. 6b).

3.3. EBSD analysis of hematite/magnetite interfaces and reduced layers

The microstructures were further analysed by EBSD to reveal the phases, grain morphology, texture and orientation relationships between the different phases. Figs. 7 and 8 show EBSD maps taken in the hematite/magnetite regions of the top and bottom basal plane facets of the 16 %-reduced sample, in projection along the $[0001]_{hem}$ (Figs. 7a–c and 8a-c) and $[1\bar{2}10]_{hem}$ directions (Figs. 7d-f and 8d), respectively. The obtained inverse pole figure (IPF) maps show a clear distinction in orientation of the grains in the cell walls and the cell interior regions, particularly when viewed in projection along $[0001]_{hem}$. The grains

within the cell interiors are strongly textured with many low angle grain boundaries (i.e. subgrains), and predominantly have the $[112]_{mag}$ axis oriented parallel to the $[0001]_{hem}$ direction. The thin black lines in the EBSD images mark grain boundaries (misorientation $>15°$).

By observing the cross-sections perpendicular to the reaction direction (i.e. in projection along $[1\bar{2}10]_{hem}$, Fig. 7d-f), it is found that the magnetite in the top basal plane facet consists of elongated grains with a roughly uniform width of $\sim$1 μm. In contrast, the elongated grains of magnetite formed at the bottom basal plane facet mostly consist of much larger grains that are $\sim$5–10 μm in width (Fig. 8d-f). These large grains are often interspersed with clusters of non-elongated, smaller grains, which originated predominantly around regions with coarse porosity (Fig. 8f). Note that wüstite formation began at a distance of roughly $\sim$7 μm from the hematite/magnetite interface in both basal planes, but present different morphologies: as either homogeneously dispersed submicron grains or clusters of subgrains in the top (Fig. 7e) and bottom (Fig. 8e) basal plane facets, respectively.

By imaging the reduced layer that originated at the bottom basal plane facet in projection along the $[0001]_{hem}$ direction, magnetite- and wüstite-rich regions can be observed (Fig. 9). These two oxides are indistinguishable in the IPF (Fig. 9c), as they exhibit a cube-on-cube orientation relationship (Fig. 9d), which is retained throughout this step in the reduction process. It is also evident that no grain refinement occurred during the transformation of magnetite to wüstite (which can be seen in Fig. 9b,c as well as in Fig. 8e,f).

When inspecting the regions rich in metallic iron using EBSD (Fig. 10), it becomes evident that the reduced iron is predominantly in contact with magnetite rather than wüstite. This contradicts the grain model expected core-shell behaviour at the micro/nanoscale [34,35], as it is expected that magnetite transforms into wüstite before being further reduced into iron at temperatures above 570 °C. Note that further grain refinement occurred upon formation of iron and that there is no texture retained once reduced to metallic iron. Furthermore, it appears that the oval cells formed in the magnetite guided the next steps in the reduction process: since the retained oxides have the same crystallographic texture as the nanoporous interior of the magnetite cells (Figs. 10c,f, and 11h), it appears that first wüstite and then iron nucleated at the weakly textured, microporous magnetite cell walls and proceeded to grow into the strongly textured, nanoporous magnetite cell interiors. The reduced layers thus present a 3D "pipe-like" morphology, with the pipe interiors consisting of iron and retained elongated iron oxide clusters. These can still be seen in both projections, particularly in the phase maps (Fig. 10c, e). This is especially evident in the bottom basal plane facet, where the textured oxides can stretch from the hematite all the way to the facet surface (Figure S6).
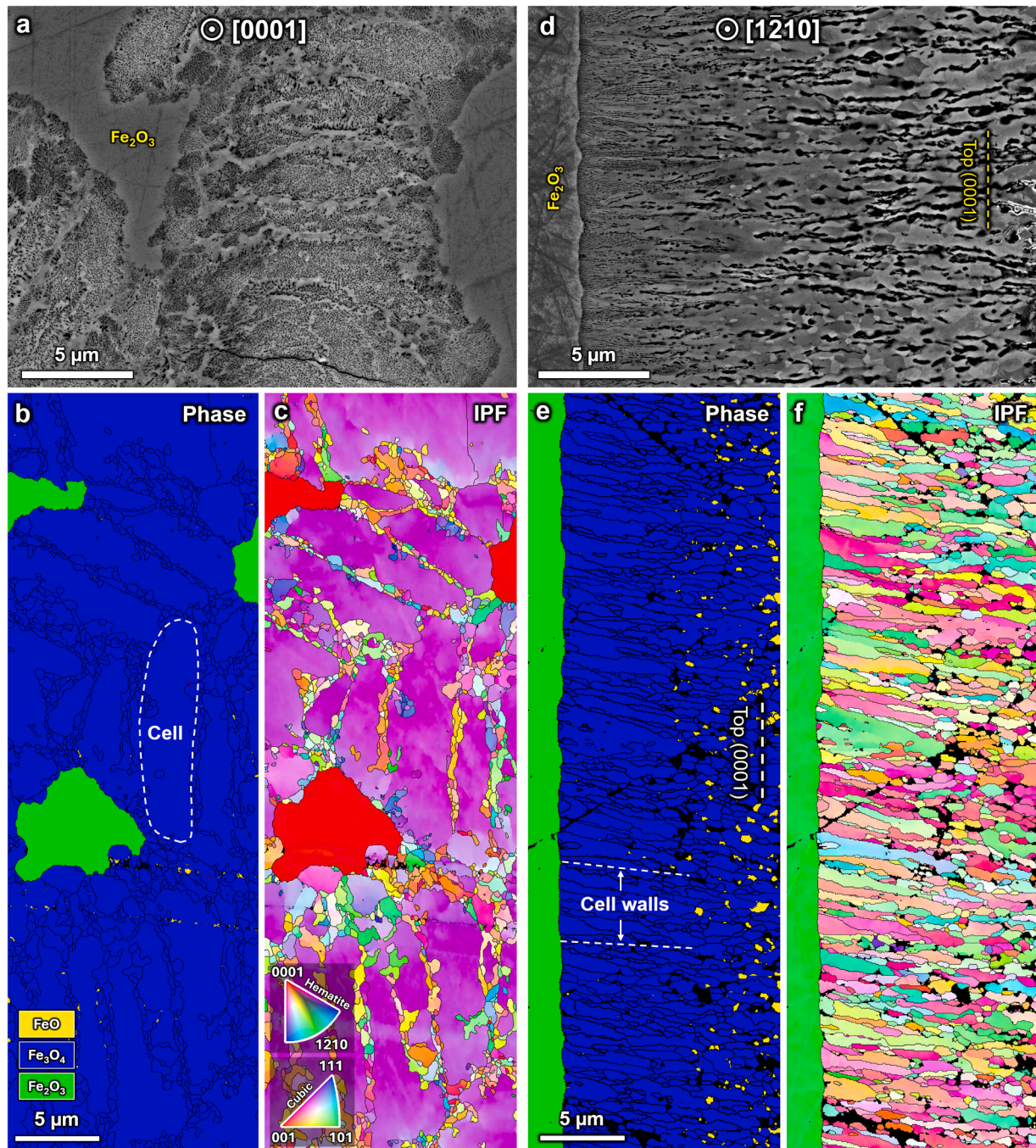
Fig. 7. EBSD analysis of the hematite/magnetite interface parallel to the top basal plane facet in the 16 %-reduced sample. (a) SEM-BSE micrograph, corresponding (b) phase map and (c) IPF for projection along the $[0001]_{hem}$ direction and (d) SEM-BSE micrograph, corresponding (e) phase map and (f) IPF for projection along the $[1\bar{2}10]_{hem}$ direction.

EBSD analysis was also performed for the $(10\bar{1}0)_{hem}$ and $(1\bar{2}10)_{hem}$ crystallographic plane facets at both the hematite/magnetite interface and within the reduced layer (Fig. 11). The microstructure of these facets appears very similar to that observed in the top basal plane facet (Fig. 7). The magnetite grains at the hematite/magnetite interface are elongated, of roughly uniform thickness, and textured (Fig. 11a–d). Additionally, there are some protrusions of metallic iron nearly reaching the hematite.

Fig. 12 presents the morphology of the hematite/magnetite interface viewed in projection along the $(1\bar{2}10)_{hem}$ plane facet in the 27 %-reduced sample. As observed for the basal plane facets, the magnetite is highly textured with the orientation depending on the original

hematite crystallographic plane facet. The cell structure is less prominent in this plane facet, but can still be observed in the smaller magnetite grains that formed between the larger ones. The cell walls can be clearly seen by visualising the IPF maps for the other axes of the sample coordinate system, [100] and [010], which can reveal their different texture as shown in Fig. 12c,d. Finally, Fig. 12e, which presents a phase map of the same sample taken further away from the hematite/magnetite interface, illustrates the formation of small equiaxed wüstite grains at the magnetite cell walls.

Fig. 13 shows the EBSD analysis of a boundary region between two reduction fronts in the 80 %-reduced sample viewed in projection along the $[1\bar{2}10]_{hem}$ direction. Such continuous oxide boundaries are
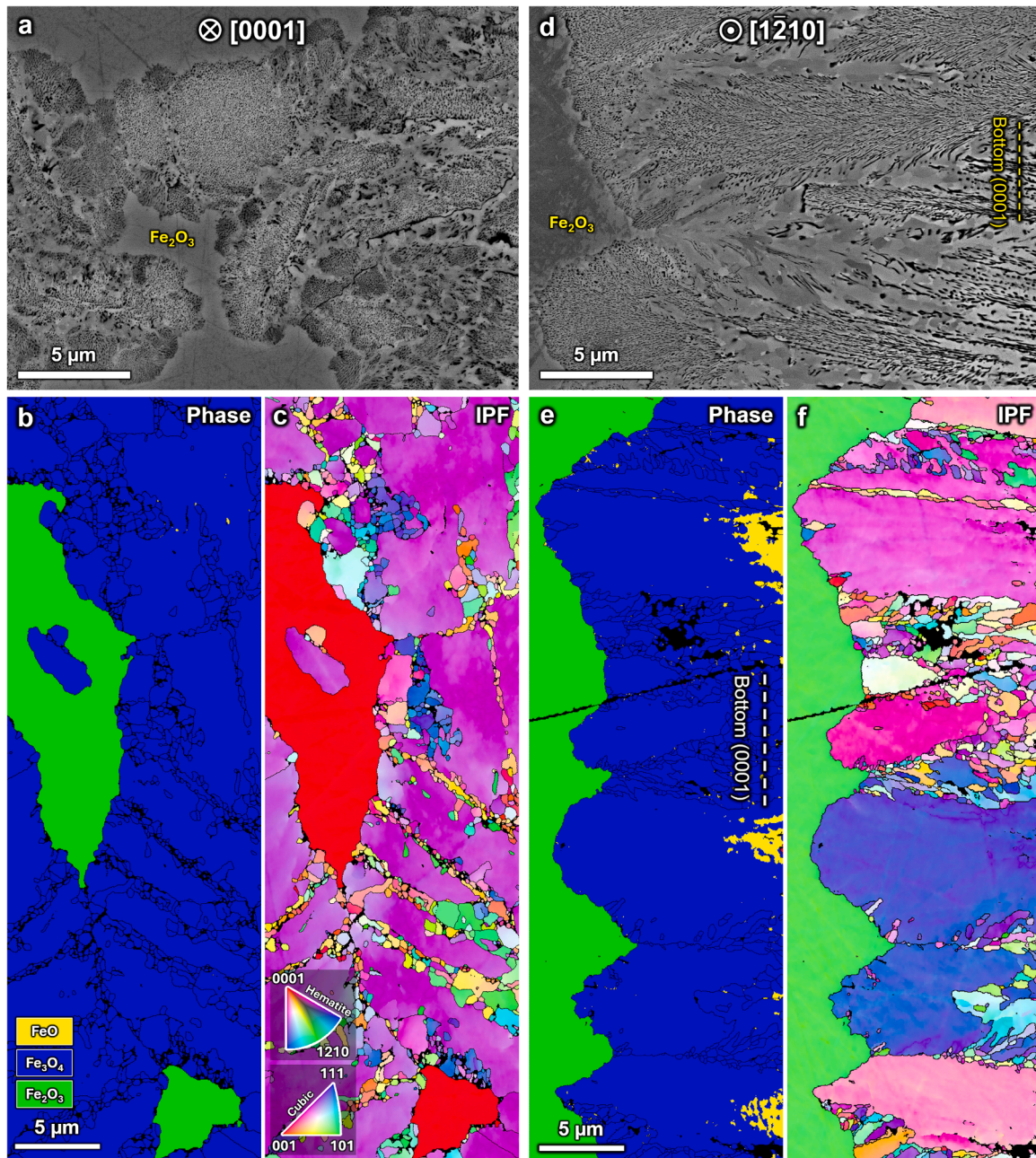
Fig. 8. EBSD analysis of the hematite/magnetite interface parallel to the bottom basal plane in the 16 %-reduced sample. (a) SEM-BSE micrograph, corresponding (b) phase map and (c) IPF for projection along the $[0001]_{hem}$ direction. (d) SEM-BSE micrograph, corresponding (e) phase map and (f) IPF for projection along the $[1\overline{2}10]_{hem}$ direction.

commonly observed throughout the sample where different reduction fronts meet. The showcased example in Fig. 13 is the meeting of the $(0001)_{hem}$ top basal and $(1\overline{2}10)_{hem}$ plane facets reduction fronts. Despite the high reduction degree, plenty of magnetite is still present, as shown in the phase map Fig. 13c. In this region, the fractions of magnetite, wüstite, and iron are determined to be 8, 13, and 79 %, respectively. These values agree with the overall 80 % reduction degree of the whole sample. Additionally, some noteworthy observations regarding the iron grains can be made: the shape of the grains displays some anisotropy, such that the average grain size appears larger in the projection perpendicular to the crystal plane facet compared with the parallel projection direction (see the lefthand and righthand side of the boundary in Fig. 13c,d). These relatively large iron grains in the top $(0001)_{hem}$ facet follow the same trend as the precursor oxide grains and exhibit

some noticeable elongation and texture. Finally, it is evident in both reduction fronts that the smaller iron grains are found in proximity to the coarse porosity while the large grains are adjacent to the retained oxide grains. These dense iron grains also surround the core of boundary regions between the reduction fronts (see other examples in Fig. 4e and S4c), which contain mainly wüstite; it is thus evident that further reduction was impeded.

4. Discussion

4.1. Single crystal reduction behaviour

The plateau in reduction rate (at 0.1 s^{-1}) of the SC sample indicates that multiple phase transformations of all oxides occurred
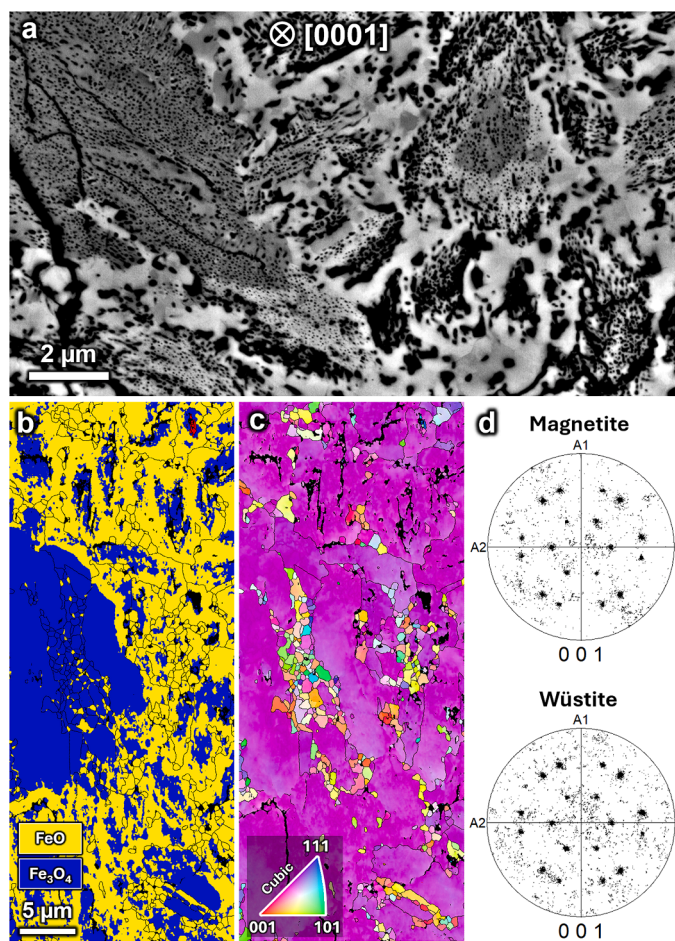
Fig. 9. EBSD analysis of a magnetite-wüstite region in the reduced layer of the bottom basal plane facet in the 16 %-reduced sample in projection along the [0001]$_{hem}$ direction. (a) Representative SEM-BSE micrograph and corresponding (b) phase map, (c) IPF, and (d) PFs of both phases.

simultaneously (up to ~30 % reduction degree), in contrast to the more sequential reduction steps of porous pellet samples (Fig. 1c). The comprehensive microstructural observations allow us to build a general picture of the direct reduction progression of iron oxide with the absence of pre-existing porosity or other defects like grain boundaries influencing the process. The HyDR of the SC can be divided into two main stages. (1) While hematite is still present, the reduction behaviour may be described by a topochemical shrinking core model [24,26,27] (Figs. 3 and 4), with the advancing reaction front leaving in its wake a porous microstructure [12] and elongated oxide grain clusters (Figs. 5-7); these likely continue to be further reduced following combined kinetics and topology features described by the pore and grain models [28]. (2) After all the hematite has transformed, reduction proceeds uniformly throughout the whole SC (abiding by the pore and grain models), aided by the outward transport of water vapour through the percolating fraction of the pore network and along microcracks (Fig. 1b insert, and Fig. 3d-f).

In stage (1), two different magnetite morphologies develop at the advancing hematite/magnetite interface, giving rise to a cell-like microstructure: the cell interior is finely porous and highly textured (for detailed discussion of orientation relationships see Section 4.4 below); conversely the cell walls contain coarse pores and exhibit weaker texture that largely differs from that of the cell interior (Figs. 7 and 8, and S7). The microstructure evolution process at the reduction front is illustrated in Fig. 14. Fig. 14a shows a planar view schematic of the hematite/magnetite interface illustrating the origin of the magnetite

cell morphology. Initially, isolated magnetite grains nucleate, and concurrently nanopores are created by an accumulation of vacancies at the hematite/magnetite interface. As these magnetite grains grow, they eventually meet adjacent magnetite grains, forming dense regions around the grain boundaries (Figure S5). Subsequently, smaller magnetite grains form in the grain boundary regions, producing further interfaces that become the preferred sites for the creation and coarsening of new pores.

During this first stage, the reduction exhibits crystallographic dependence, as suggested by the fact that the reduction progressed towards the sample core roughly 10 % more quickly from the (0001)$_{hem}$ basal plane facets than from the (10$\bar{1}$0)$_{hem}$ and (1$\bar{2}$10)$_{hem}$ facets. As illustrated in Fig. 14b, the initial magnetite cells subsequently develop into pipe-like structures with expanding metallic iron interspersed with iron oxide (Fig. 10). Thus, the magnetite cell walls surrounded by coarse pores serve as the primary and accelerated wüstite and iron nucleation sites, which then continue to expand inward into the textured magnetite. The fact that much of the iron is found adjacent to magnetite somewhat contradicts thermodynamic intuition as well as the presumed grain model reduction sequence (localised shrinking core model for individual grains) [34,35], in that wüstite is often absent. In this context it is worth noting, as outlined above (Fig. 9), that magnetite and wüstite are observed to occur in an isostructural pattern, with no change in crystal orientation. This suggests that the nucleation of wüstite is associated with overcoming a low energy barrier, requiring only minimal distortion of the magnetite oxygen lattice.

In stage (2), the reduction behaviour is expected to continue to follow the same combination of the pore and grain model behaviours, aided by the percolating pore network (Figs. 10,11e-h, S6); this stage is governed by solid-state diffusion of oxygen through the growing iron layer and outward gas diffusion of water vapour. After 80 % reduction, the SC still possesses abundant oxides distributed throughout the whole sample (roughly 2:1 wüstite to magnetite ratio). This is due to the encapsulation of elongated oxide clusters by iron as iron nuclei expand from the magnetite cell walls as outlined in stage (1). This local core-shell behaviour hinders the outbound diffusion of oxygen through the dense iron layer, as the diffusion coefficient of oxygen in iron is small. Additionally, the retention of oxides could further hinder outward mass transport during the late stages of reduction (note that the oxides are retained even in the 80 %-reduced sample) due to lower diffusion coefficients of O inside the oxides compared to metallic iron. Specifically, the diffusivity of O in magnetite (10^{-18}–10^{-17} m^2/s) [36,37] is comparable to that of O in non-stoichiometric wüstite (~10^{-18} m^2/s) [38], both low with respect to the diffusivity of O in iron (10^{-14}–10^{-11} m^2/s) [39,40]. Overall, it is apparent that during this second stage, the reduction of the SC proceeds homogeneously throughout the depth of the sample. The aforementioned trend that the basal planes reduce more effectively than the other plane facets is also reflected by their higher iron to oxide ratios, see Section 3.2 (Figs. 3d,e and 4 g,h). Note that in some regions the material becomes considerably dense (due to sintering), decreasing the effectiveness of the percolating pore network that is critical for internal gas diffusion; this may explain the extremely sluggish final Fe$_{1-x}$O→Fe step. In particular, water vapour might be trapped in the closed pores, reducing the partial pressure of hydrogen or even leading to reoxidation of reduced iron to wüstite [10,41,42].

4.2. Nanopore channel formation at the hematite/magnetite interface

Reduction of hematite to magnetite results in the formation of a network of nanoscale pore channels near the hematite/magnetite interface [21]. These pores coalesce in the following reduction steps, i.e. to wüstite and iron (Fig. 5). The formation of this hierarchical porous structure is likely a critical factor in determining how the reduction progresses throughout the bulk SC sample. The nanoscale pore channel diameters and distance between adjacent pores were determined by
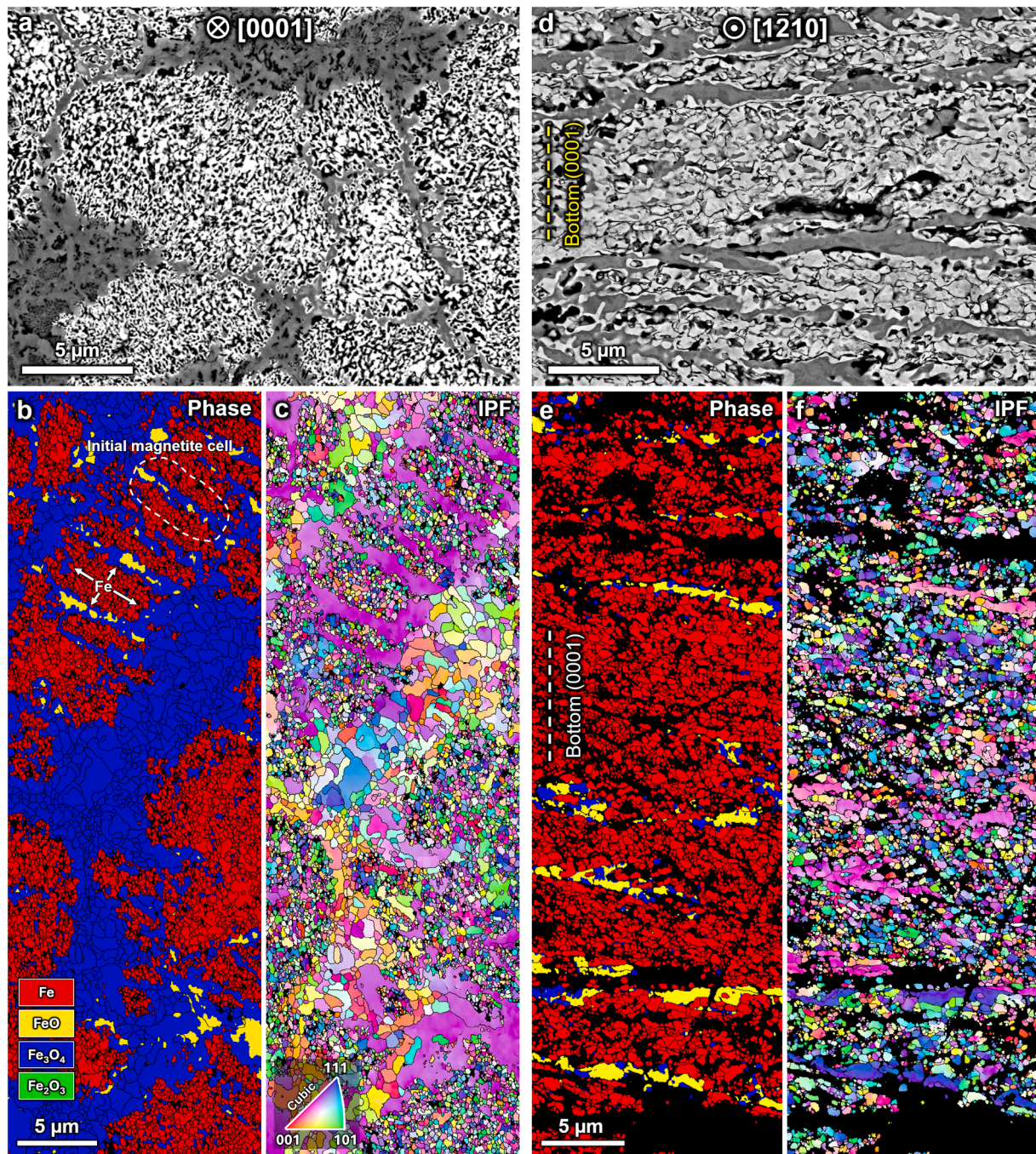
Fig. 10. EBSD analysis of iron-rich zones in the reduced layer of the bottom basal plane facet in the 16 %-reduced sample. (a) SEM-BSE micrographs and corresponding (b) phase map and (c) IPF in projection along the $[0001]_{hem}$ direction. (d) SEM-BSE micrograph and corresponding (e) phase map and (f) IPF in projection along the $[1\bar{2}10]_{hem}$ direction.

image analysis (see Figs. 5 and S5) for the magnetite region closest to the hematite interface in the 16 %-reduced sample. The pore size and distance distributions obtained from the $(10\bar{1}0)_{hem}$ plane facet and the two basal plane facets, in projection along $[10\bar{1}0]_{hem}$ and $[0001]_{hem}$, respectively, are shown in Fig. 15. The nanopore channels extend up to ~2–4 μm in length before coarsening (Fig. 5a,b), and have spherical/oval cross-sections (Fig. 5c) with mean diameters of ~28–35 ± 10 nm near the hematite (Fig. 15a-c). Furthermore, the average distance between the pores in these regions is ~70–80±20 nm (Fig. 15d-f). Similar observations of nanopore formation in magnetite at the hematite/magnetite interface have been reported by Swann & Tighe [12] for a hematite SC reduced by CO, although the pores observed by these

authors had a more uniform distribution with smaller diameters (~6–10 nm), and distances (~35 nm). The reasons behind these differences may be related to the temperature and reducing atmosphere as well as the geometry of the SC employed in the experiments, as in that study reduction was carried out at a significantly lower temperature of 400 °C and the samples were much thinner SC plates (40 μm in thickness), in contrast to the 700 °C reduction temperature and 2 mm-thick samples in the present study.

The pore sizes and their distances are similar in the $(10\bar{1}0)_{hem}$ plane and top basal plane facets, while the pores in the bottom basal plane facet are larger by ~15 % as well as ~20 % closer to one another. This result suggests that the gas flow conditions at the bottom basal plane
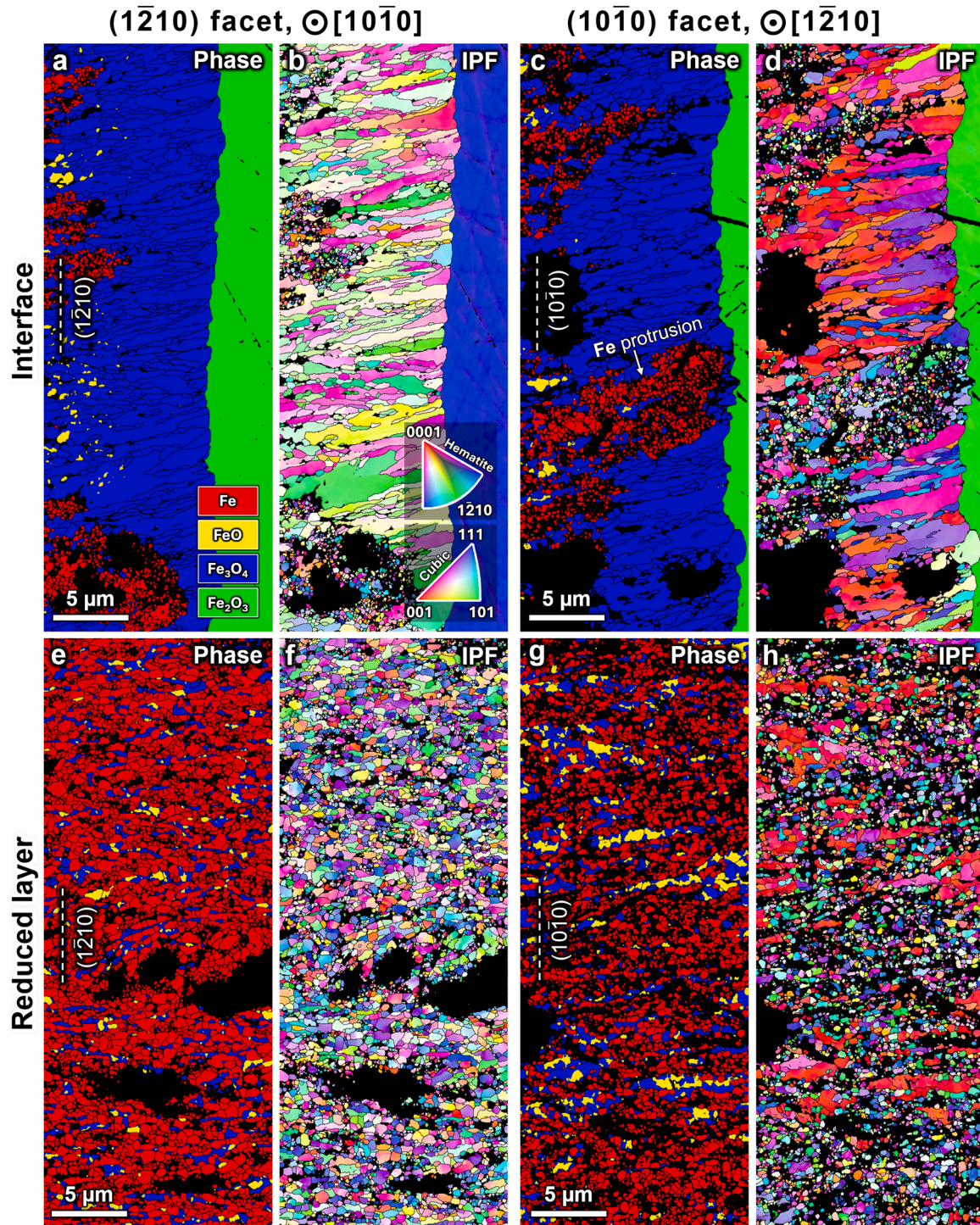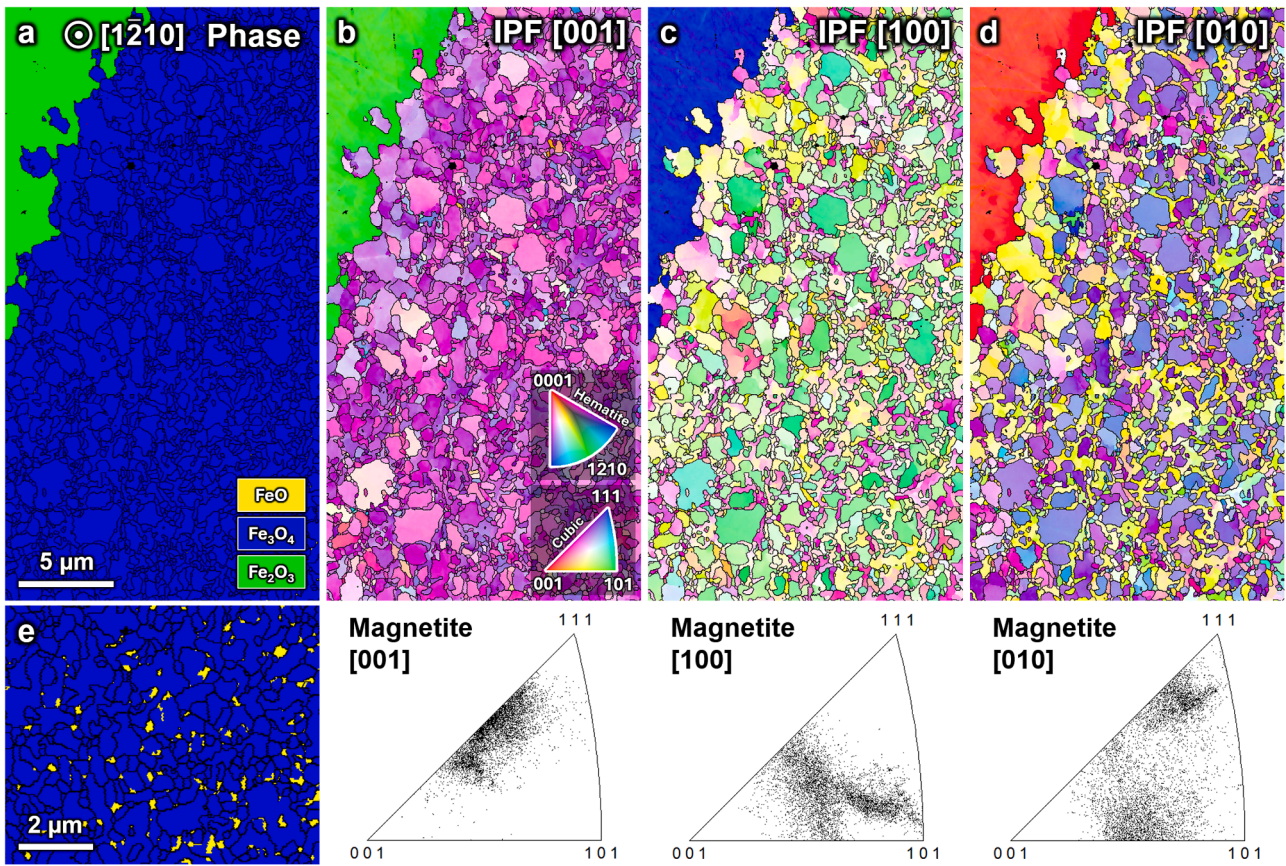
Fig. 11. EBSD analysis of the $(1\bar{2}10)_{hem}$ and $(10\bar{1}0)_{hem}$ plane facets in the 16 %-reduced sample. Hematite/magnetite interface: (a) phase map and (b) IPF parallel to the $(1\bar{2}10)_{hem}$ plane facet viewed in projection along $[10\bar{1}0]_{hem}$; (c) phase map and (d) IPF parallel to the $(10\bar{1}0)_{hem}$ plane facet viewed in projection along $[1\bar{2}10]_{hem}$. Reduced layer: (e) phase map and (f) IPF of the $(1\bar{2}10)_{hem}$ plane facet viewed in projection along $[10\bar{1}0]_{hem}$; (g) phase map and (h) IPF of the $(10\bar{1}0)_{hem}$ plane facet viewed in projection along $[1\bar{2}10]_{hem}$.

facet led to the formation of a higher number density of nanoscale pores, which would have accelerated the subsequent reduction step, i.e. magnetite to wüstite, in the textured magnetite regions; this may explain in part the difference in magnetite grain morphology observed in the top and bottom basal plane facets (Figs. 7 and 8).

4.3. Phase and porosity evolution in the reduction layer

The porosity and phase fractions across the reduced layer as a function of distance from the hematite/magnetite interface are plotted in Fig. 16 for each of the crystallographic plane facets in the 16 %-reduced sample. A region with a width of >10 μm was analysed across the length of the interface. The line profiles reveal the correlation

Fig. 12. EBSD analysis of the $(1\bar{2}10)_{hem}$ plane facet hematite/magnetite interface in the 27 %-reduced sample in projection along $[1\bar{2}10]_{hem}$ direction. (a) Phase map and IPF maps for (b) [001], (c) [100], and (d) [010] axes of the sample, with the corresponding magnetite PF plots for each direction included below. The difference in texture between the magnetite cell interiors and walls can be most clearly observed in the [010] IPF map. (e) Phase map of an area further away from the hematite/magnetite interface showing the formation of wüstite grains at the magnetite cell walls.
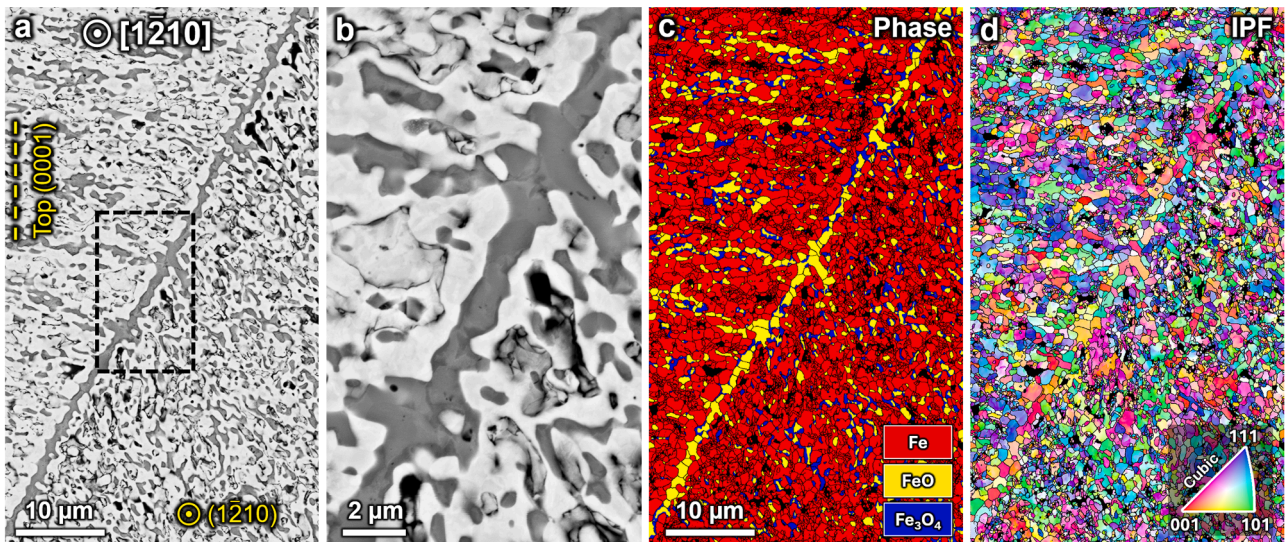

Fig. 13. EBSD analysis of a boundary region between two reduction fronts in the 80 %-reduced sample viewed along $[1\bar{2}10]_{hem}$. The reduced layer initially originated at the $(1\bar{2}10)_{hem}$ (righthand side of the boundary) and top $(0001)_{hem}$ plane (lefthand side) facets. (a) SEM-BSE micrograph of the boundary region. (b) Higher magnification of the region marked with the dashed rectangle in (a); the bright and dark grey phases are wüstite and magnetite, respectively. EBSD (c) phase map and (d) IPF micrographs corresponding to the region in (a).

between phase transformation and the formation of pores, highlighting the differences between the various crystallographic plane facets. Examples of porosity micrographs created by image analysis are shown in

Figure S8 (and the iron fraction was similarly measured). Regarding the porosity development, all plane facets share a similar trend. Fine pores nucleate following the accumulation of vacancies in the magnetite close
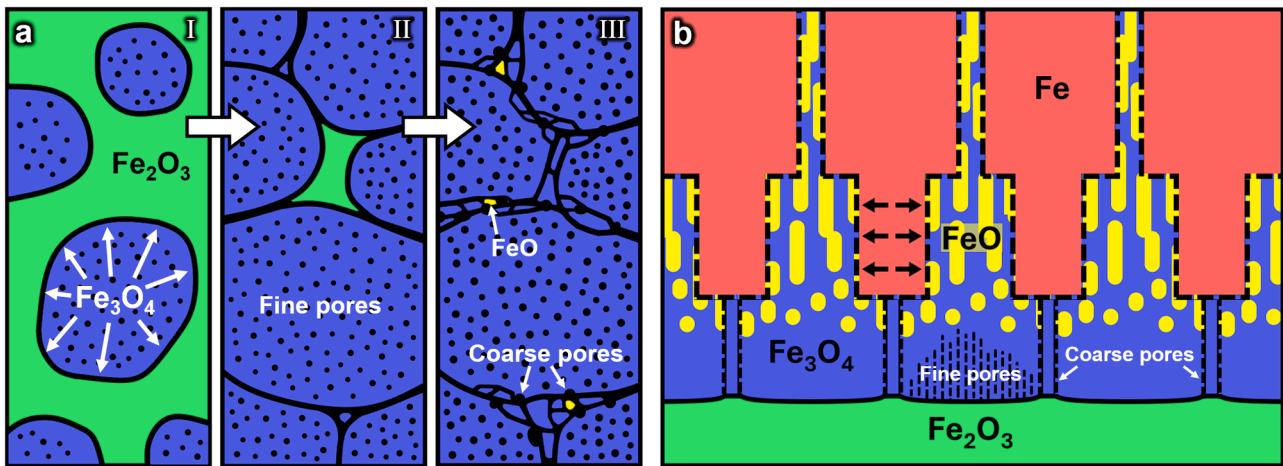
Fig. 14. Schematic illustration of the microscale reduction front development. (a) Planar view of the initial stages at the hematite/magnetite interface depicting (I) formation of textured porous magnetite grains in the hematite, (II) followed by their growth to create the "cell morphology", and (III) ensuing coarsening of pores alongside formation of smaller magnetite grains. The small magnetite grains in porous regions are eventually the first to transform into wüstite and initiate Fe nucleation. (b) Formation of the reduction layer in cross-sectional view, depicting the sequential transformation from Fe_2O_3 to Fe; black arrows indicate the outward expansion of Fe from the initial nucleation sites at magnetite cell walls into the cell interiors.
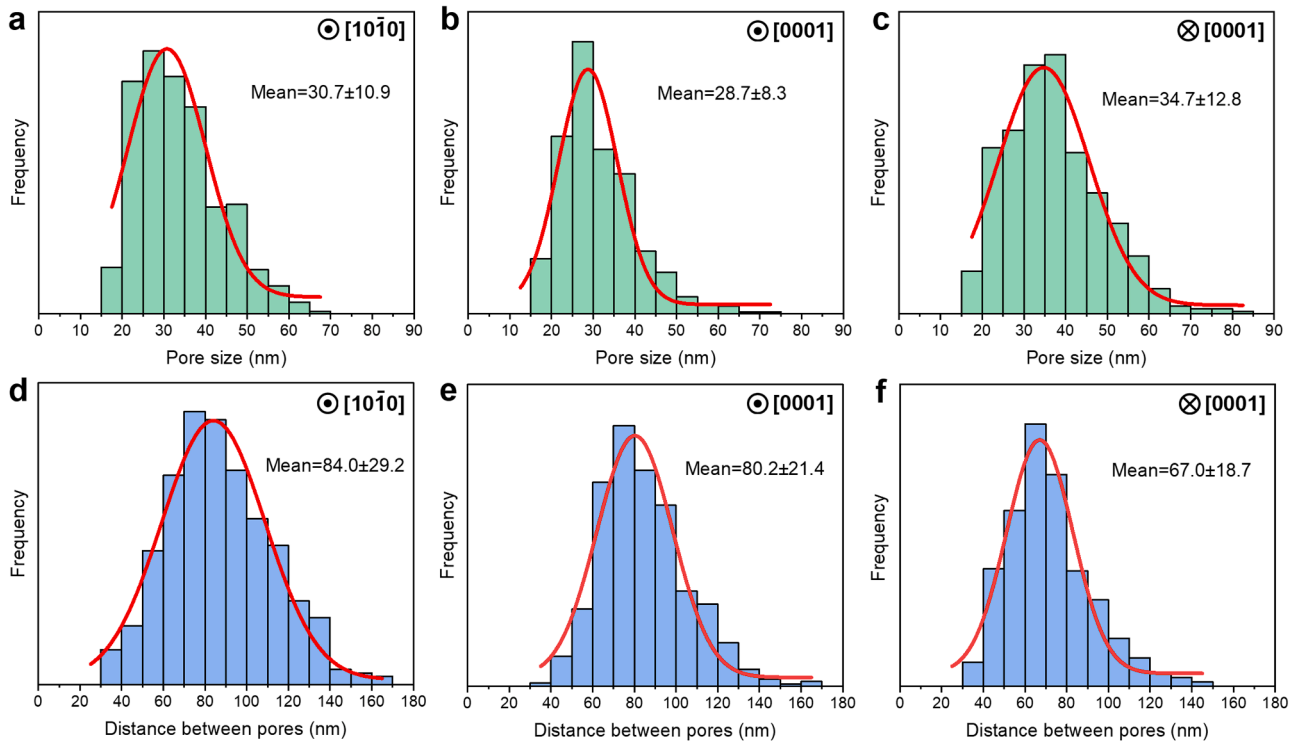

Fig. 15. Pore analysis at the hematite/magnetite interfaces in the 16 %-reduced sample. Pore diameter distributions of the (a) $(10\bar{1}0)_{hem}$ plane facet (projection along $[10\bar{1}0]_{hem}$), (b) top basal $(0001)_{hem}$ and (c) bottom basal $(0001)_{hem}$ plane facets (projection along $[0001]_{hem}$ for both basal planes). Pore distance distributions of the (d) $(10\bar{1}0)_{hem}$, (e) top basal $(0001)_{hem}$ and (f) bottom basal $(0001)_{hem}$ plane facets.

to the hematite, and form channels with a hierarchal morphology wherein as the reduction progresses, larger and more interconnected voids are created. In the vicinity of the reaction interface, i.e. in the magnetite adjacent to the hematite, the porosity fraction starts at ~10 %, then it increases up to ~25 %, followed by a slight decrease to ~15–25 %. The porosity in the reduced region away from the proceeding hematite/magnetite interface remains ~15–25 % (discounting the large irregular pores that sometimes develop due to the fast reaction close to the SC facet surface). Similar behaviour and a ~15–20 % porosity fraction were reported in the reduction of hematite to

magnetite [19]. Furthermore, in all the crystal plane facets the porosity peaks in the environs of the onset of metallic iron formation, consistently with the large volume change associated with the transformation (~41 % contraction for bcc iron relative to fcc wüstite, based on atomic volume). Another common trait is that at ~50 μm from the hematite/magnetite interface the fractions of porosity/oxides/iron plateau and remain roughly constant across the rest of the reduced layer.

On the other hand, several differences among the crystallographic plane facets are noticeable. First, metallic iron forms closer to the hematite/magnetite interface in the $(10\bar{1}0)_{hem}$ and $(1\bar{2}10)_{hem}$ plane facets
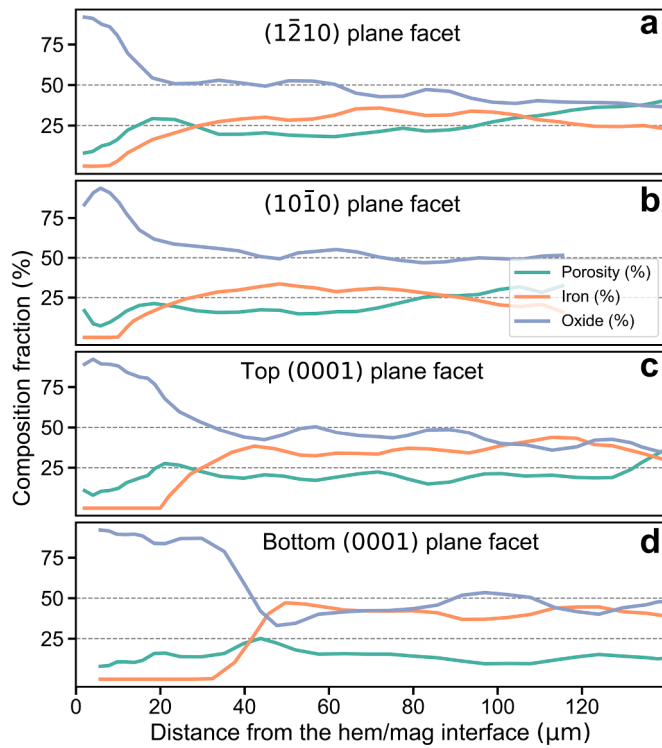
Fig. 16. Line profiles of the porosity and phase composition obtained by image analysis of the reduction layers originated from each of the plane facets in the 16 %-reduced sample. (a) $(1\bar{2}10)_{hem}$ facet, (b) $(10\bar{1}0)_{hem}$ facet, (c) top $(0001)_{hem}$ facet, and (d) bottom $(0001)_{hem}$ facet. All images analysed were collected along the $[1\bar{2}10]_{hem}$ projection direction, except (a), where images were collected along the $[10\bar{1}0]_{hem}$ projection direction.

($\sim$10 μm from the interface) compared to the basal plane facets ($\sim$20 and 30 μm from the interface at the top and bottom basal plane facets, respectively). Second, the rates of iron fraction increase show a corresponding trend: the iron fraction in the $(10\bar{1}0)_{hem}$ and $(1\bar{2}10)_{hem}$ plane facets reaches a maximum over the span of $\sim$40 μm, while the iron content in the basal plane facets peaks at $\sim$20 μm from the interface in the top and bottom basal planes. Third, the maximum iron fraction is $\sim$30 % for the $(10\bar{1}0)_{hem}$ and $(1\bar{2}10)_{hem}$ plane facets, while it reaches almost 40 and 45 % in the top and bottom basal plane facets, respectively. Finally, as the iron and oxide fractions reach their maxima and plateau, in the $(1\bar{2}10)_{hem}$ and $(10\bar{1}0)_{hem}$ plane facets the iron content remains lower than the oxide content (by $\sim$35 % and $\sim$50 % on average, respectively), whilst in the top and bottom basal plane facets the two fractions are roughly equal.

4.4. Orientation relationships at the hematite/magnetite interface

Previous studies established that reduction temperature influences the microstructure evolution during the reaction, particularly in the hematite to magnetite reduction step. Lenticular magnetite formations are typically observed at higher temperatures ($\geq$800 °C) [12,15], and they exhibit the Shoji-Nishiyama (S-N) orientation relationship (OR) with hematite: that is $(111)_{mag}//(0001)_{hem}$ and $[1\bar{1}0]_{mag}//[10\bar{1}0]_{hem}$, a variation (due to the fact that hematite has a corundum structure with trigonal symmetry) of the typically expected OR between fcc and hexagonal crystal structures [43]; the interface between hematite and magnetite in this case is thought to be semicoherent [13]. At lower temperatures (up to $\sim$650 °C), porous spherical or cellular magnetite nuclei are observed [12,15], and are associated with a broader spectrum of ORs, with one OR presenting $(112)_{mag}//(0001)_{hem}$ and $[1\bar{1}0]_{mag}//[10\bar{1}0]_{hem}$ (henceforth OR2) being observed more often [44, 45]; this OR is thought to be associated with an incoherent hematite/magnetite interface [46]. It should also be noted that a variation in OR was observed at different depths in the magnetite layer covering a hematite SC in the work of El Abdouni et al. [16]. The authors observed that magnetite closer to the surface of the sample commonly exhibited
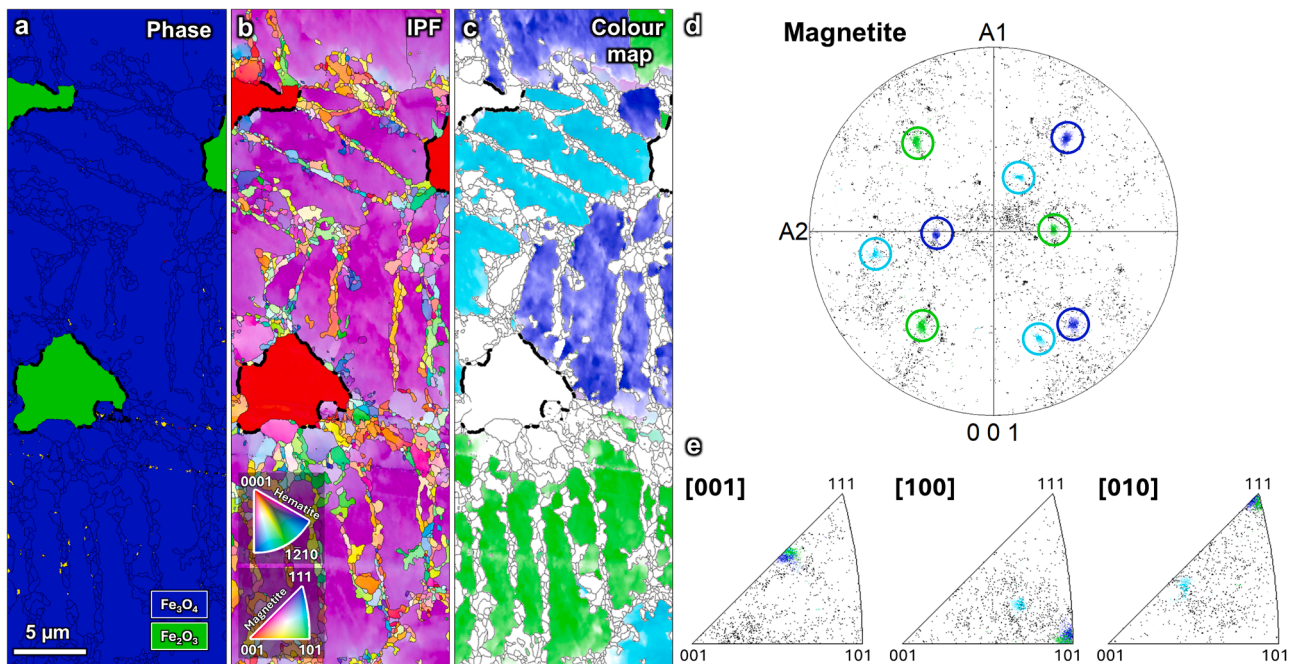
Fig. 17. OR2 analysis by EBSD of the hematite/magnetite interface in the top basal plane facet of the 16 %-reduced sample viewed in the $[0001]_{hem}$ projection. The length of interface between hematite and magnetite abiding by OR2 is marked with a bold black line (with a tolerance of up to 10°). EBSD (a) phase (b) IPF and (c) colour maps. The colours in (c) correspond to the respective OR2 variants shown in the (d) PF and (e) matching IPF plots for different sample orientations. The lighter shades in the colour maps depict the deviation of the subgrains from the exact orientation (with a tolerance of up to 5°).

S-N OR with the unreduced hematite core, while OR2 was mostly observed closer to the hematite/magnetite interface. An "intermediate" OR was also observed in the magnetite bulk, creating a gradient in the orientation of the magnetite from the surface to the hematite interface. As the depth of the magnetite layer is linked to the reduction degree, it was proposed that the S-N OR appeared at the early stages of reduction when a thin magnetite layer was first formed, but was then substituted by OR2 as the reaction progressed and the magnetite layer thickened.

In the present study, an abundance of OR2 is observed, particularly in the basal plane facets, but also in the $(10\overline{1}0)_{hem}$ and $(1\overline{2}10)_{hem}$ facets. This is illustrated in the IPF maps of the basal plane facets taken in projection along $[0001]_{hem}$, Figs. 6c and 7c, and from the magnetite PF of Fig. 8d, showing a splitting of the basal pole into 18 poles, each corresponding to a variant of magnetite following OR2 [44]. Nine of these variants are highlighted in Fig. 17. This shows the same region as Fig. 7b,c, i.e. an area at some depth in the top basal plane facet containing hematite and magnetite, viewed in projection along $[0001]_{hem}$, albeit with the addition of a colour map, coded according to the variant of OR2 displayed by the magnetite grains. The orientation of each of the nine variants can be seen in the PF (Fig. 17d): they comprise three sets of three identical variants by cubic symmetry, with one colour assigned to each set. The three geometrically distinct but equivalent sets are further pointed out with the same colour coding in the IPF plots for each sample direction (Fig. 17e). The length of hematite/magnetite interface following OR2 is denoted by thick black lines in the phase, IPF and colour maps, with a tolerance of 10° allowed for parallel planes and directions. In contrast, the S-N OR is rarely observed in this study: not at all in the basal plane facets and only ~10 % of the hematite/magnetite interfaces in the other plane facets. This morphology was obtained at 700 °C: this may be considered an intermediate reduction temperature, in the transition region between the cellular and lamellar magnetite morphologies observed in the literature. However, the absence of magnetite with S-N OR suggests that the lenticular magnetite regime was not entered. Instead, magnetite with fine pores largely obeying OR2 and presenting the expected cellular morphology is surrounded by denser oxide presenting more complex ORs, i.e. the cell walls (Fig. 17). While the top and bottom basal plane facets present different cell sizes, pore sizes and pore distance distributions, as shown in Section 4.2, they display similar cell-like morphologies. The specific role played by OR2 is however not yet well understood, nor are the reasons for the prevalence of OR2 over S-N OR in the SC considered in this study; further investigation of the reduction mechanisms at the reaction interface down to the nanoscale is thus needed.

5. Conclusions

In the present study, single crystal (SC) hematite was used as a model system to elucidate the fundamental phase transformation, pore formation, transport, and crystallographic evolution mechanisms that altogether shape the complex microstructures forming during hydrogen-based direct reduction at 700 °C. Despite the absence of any pre-existing porosity (a characteristic of all studies done on sintered pellets), a percolating pore network rapidly forms in the sample and facilitates the reduction process throughout the bulk of the sample (>90 % reduced in 1 h). The main crystallographic plane facets, i.e. $(10\overline{1}0)_{hem}$, $(1\overline{2}10)_{hem}$, and $(0001)_{hem}$, were examined after partial reduction of SC samples to 16 % and 80 %. The main conclusions are summarised as follows:

- The reduction followed a macroscopic shrinking core behaviour only during the initial conversion of hematite into magnetite (a layer of which always separates the unreacted core from the reduced frame); the reduced layer then comprised a mixture of oxides and metallic iron, with a sizeable portion of magnetite retained (as ~30 % of the total oxide phases) throughout the sample even in the late stage of reduction (>80 % metallic iron).

- The reduction progressed roughly 10 % more quickly perpendicular the $(0001)_{hem}$ basal plane facets as compared to the $(10\overline{1}0)_{hem}$, $(1\overline{2}10)_{hem}$ plane facets.

- The magnetite formed at the reaction front presented porous cell-like structures, consisting of strongly textured inner regions with fine nanopore channels surrounded by magnetite grains with weaker texture and coarse pores. The latter, termed "cell walls", served as nucleation sites for metallic iron to grow into the cell interiors.

- The different crystallographic facets exhibited similar morphologies except for the bottom basal plane facet, which developed oxide/iron streaks and larger magnetite grains with denser and larger pores (by ~20 %). This behaviour was attributed to different gas flow conditions that developed at the bottom of the sample.

- Analysis of the porosity/oxide/iron fractions in the 16 %-reduced sample across the reduced layers of the different crystallographic facets revealed that: (1) the distance between the onset of iron formation and the hematite/magnetite interface was relatively small in the $(10\overline{1}0)_{hem}$ and $(1\overline{2}10)_{hem}$ facets (~10 μm), and larger for the $(0001)_{hem}$ basal plane facets (~20 and ~30 μm for the top and bottom facets, respectively); (2) in all facets the porosity profiles showed a similar trend, peaking shortly after the onset of iron formation; (3) in all facets at a distance of ~50 μm from the hematite/ magnetite interface the porosity/oxide/iron fractions nearly plateaued until they diverged close to the surface.

- The Shoji-Nishiyama OR was not commonly observed for the hematite/magnetite interfaces and instead the dominant OR was $(112)_{mag}//(0001)_{hem}$ and $[1\overline{1}0]_{mag}//[10\overline{1}0]_{hem}$, into which further investigation is needed.

Overall, the findings of this study provide fundamental insights into the reduction behaviour of hematite, particularly relevant to dense regions that can be found in commercial pellets or natural ore.

CRediT authorship contribution statement

Barak Ratzker: Writing – review & editing, Writing – original draft, Visualization, Methodology, Investigation, Formal analysis, Conceptualization. **Martina Ruffino:** Writing – review & editing, Writing – original draft, Visualization, Methodology, Investigation, Formal analysis, Conceptualization. **Shiv Shankar:** Investigation, Formal analysis. **Dierk Raabe:** Writing – review & editing, Supervision, Resources, Funding acquisition. **Yan Ma:** Writing – review & editing, Supervision, Funding acquisition.

Declaration of competing interest

The authors declare that they have no known competing financial interests or personal relationships that could have appeared to influence the work reported in this paper.

Acknowledgements

reflect those of the European Union the ERC. Neither the European Union nor the granting authority can be held responsible for them.

Supplementary materials

Supplementary material associated with this article can be found, in the online version, at doi:10.1016/j.actamat.2025.121174.

References

[1] D. Raabe, C.C. Tasan, E.A. Olivetti, Strategies for improving the sustainability of structural metals, Nature 575 (2019) 64–74, https://doi.org/10.1038/s41586-019-1702-5.

[2] D. Spreitzer, J. Schenk, Reduction of iron oxides with hydrogen—a review, Steel Res. Int. 90 (2019) 1900108, https://doi.org/10.1002/srin.201900108.

[3] R.R. Wang, Y.Q. Zhao, A. Babich, D. Senk, X.Y. Fan, Hydrogen direct reduction (H-DR) in steel industry—an overview of challenges and opportunities, J. Clean. Prod. 329 (2021) 129797, https://doi.org/10.1016/j.jclepro.2021.129797.

[4] Z. Miškovičová, J. Legemza, P. Demeter, B. Buľko, S. Hubatka, M. Hrubovčáková, P. Futáš, R. Findorák, An overview analysis of current research status in iron oxides reduction by hydrogen, Metals (Basel). 14 (2024) 589, https://doi.org/10.3390/met14050589.

[5] M.F. Rau, D. Rieck, J.W. Evans, Investigation of iron oxide reduction by TEM, Metall. Trans. B. 18 (1987) 257–278, https://doi.org/10.1007/BF02658451.

[6] P. Cavaliere, A. Perrone, L. Dijon, A. Laska, D. Koszelow, Direct reduction of pellets through hydrogen: experimental and model behaviour, Int. J. Hydrogen Energy. 49 (2024) 1444–1460, https://doi.org/10.1016/j.ijhydene.2023.11.040.

[7] B. Sadeghi, M. Najafizadeh, P. Cavaliere, A. Shabani, M. Aminaei, Effect of composition and processing conditions on the direct reduction of iron oxide pellets, Powder Technol 444 (2024) 120061, https://doi.org/10.1016/j.powtec.2024.120061.

[8] S.H. Kim, X. Zhang, Y. Ma, I.R. Souza Filho, K. Schweinar, K. Angenendt, D. Vogel, L.T. Stephenson, A.A. El-Zoka, J.R. Mianroodi, M. Rohwerder, B. Gault, D. Raabe, Influence of microstructure and atomic-scale chemistry on the direct reduction of iron ore with hydrogen at 700 °C, Acta Mater 212 (2021) 116933, https://doi.org/10.1016/j.actamat.2021.116933.

[9] Y. Ma, I.R. Souza Filho, Y. Bai, J. Schenk, F. Patisson, A. Beck, J.A. van Bokhoven, M.G. Willinger, K. Li, D. Xie, D. Ponge, S. Zaefferer, B. Gault, J.R. Mianroodi, D. Raabe, Hierarchical nature of hydrogen-based direct reduction of iron oxides, Scr. Mater. 213 (2022) 114571, https://doi.org/10.1016/j.scriptamat.2022.114571.

[10] A.A. El-Zoka, L.T. Stephenson, S.H. Kim, B. Gault, D. Raabe, The fate of water in hydrogen-based iron oxide reduction, Adv. Sci. 10 (2023) 2300626, https://doi.org/10.1002/advs.202300626.

[11] Y. Ma, I.R. Souza Filho, X. Zhang, S. Nandy, P. Barriobero-Vila, G. Requena, D. Vogel, M. Rohwerder, D. Ponge, H. Springer, D. Raabe, Hydrogen-based direct reduction of iron oxide at 700 °C: heterogeneity at pellet and microstructure scales, Int. J. Miner. Metall. Mater. 29 (2022) 1901–1907, https://doi.org/10.1007/s12613-022-2440-5.

[12] P.R. Swann, N.J. Tighe, High-voltage microscopy of reduction of hematite to magnetite, Metall. Trans. B. 8 (1977) 479–487, https://doi.org/10.1007/BF02696936.

[13] P.C. Hayes, P. Grieveson, Microstructural changes on the reduction of hematite to maanetite, Metall. Trans. B. 12 (1981) 579–587, https://doi.org/10.1007/BF02654330.

[14] M. Ettabirou, B. Dupré, C. Gleitzer, Nucleation and early growth of magnetite on synthetic and natural hematite crystals, React. Solids. 1 (1986) 329–343, https://doi.org/10.1016/0168-7336(86)80025-0.

[15] M. Et-Tabirou, B. Dupré, C. Gleitzer, Hematite single crystal reduction into magnetite with CO-CO₂, Metall. Trans. B. 19 (1988) 311–317, https://doi.org/10.1007/BF02654216.

[16] H. El Abdouni, A. Modaressi, J.J. Heizmann, The changes in texture during the reduction of hematite to magnetite. Kinetic study of the phase transformation at 650 °C, React. Solids. 5 (1988) 129–138, https://doi.org/10.1016/0168-7336(88)80082-2.

[17] F. Adam, F. Jeannot, B. Dupre, C. Glettzer, The remarkable effect of water vapour on the cracking of hematite during its reduction into magnetite, React. Solids. 5 (1988) 115–127, https://doi.org/10.1016/0168-7336(88)80081-0.

[18] J. Janowski, M. Wyderko-Delekta, A. Sadowski, J. Delekta, Morphology of hematite to magnetite reduction zone, Steel Res 66 (1995) 135–139, https://doi.org/10.1002/srin.199501101.

[19] J. Janowski, A. Barański, A. Sadowski, Porosity profiles in emerging magnetite layer during the reduction of hematite, Solid State Ionics 101–103 (1997) 807–810, https://doi.org/10.1016/s0167-2738(97)00296-6.

[20] T. Simmonds, P.C. Hayes, Reduction of hematite to magnetite in CO/CO₂ gas mixtures under carbon looping combustion conditions, Metall. Mater. Trans. E. 4 (2017) 101–113, https://doi.org/10.1007/s40553-017-0112-6.

[21] J. Chen, R. Zhang, T. Simmonds, P.C. Hayes, Microstructural changes and kinetics of reduction of hematite to magnetite in CO/CO₂ gas atmospheres, Metall. Mater.

[22] M. Bahgat, M.H. Khedr, Reduction kinetics, magnetic behavior and morphological changes during reduction of magnetite single crystal, Mater. Sci. Eng. B. 138 (2007) 251–258, https://doi.org/10.1016/j.mseb.2007.01.029.

[23] W.M. Husslage, T. Bakker, M.E. Kock, R.H. Heerema, Influence of reduction conditions on the expansion and microtexture of sintered hematite compacts during the transition to magnetite, Miner. Metall. Process. 16 (1999) 23–33, https://doi.org/10.1007/bf03402815.

[24] G. Bitsianes, T.L. Joseph, Topochemical aspects of iron ore reduction, JOM 7 (1955) 639–645, https://doi.org/10.1007/bf03377553.

[25] E.H. Ahra, A. Modaressi, J. Bessieres, J.J. Heizmann, Kinetic laws for parallelepipedic samples of hematite during their topochemical reduction to magnetite, Solid State Ionics 81 (1995) 5–14, https://doi.org/10.1016/0167-2738(95)00174-5.

[26] E.T. Turkdogan, J.V. Vinters, Gaseous reduction of iron oxides: part I. Reduction of hematite in hydrogen, Metall. Trans. 2 (1971) 3175–3188, https://doi.org/10.1007/bf02814970.

[27] Q.T. Tsay, W.H. Ray, J. Szekely, The modeling of hematite reduction with hydrogen plus carbon monoxide mixtures: part II. The direct reduction process in a shaft furnace arrangement, AIChE J 22 (1976) 1072–1079, https://doi.org/10.1002/aic.690220618.

[28] J. Szekely, J.W. Evans, A structural model for gas-solid reactions with a moving boundary, Chem. Eng. Sci. 25 (1970) 1091–1107, https://doi.org/10.1016/0009-2509(70)85053-9.

[29] M. Auinger, D. Vogel, A. Vogel, M. Spiegel, M. Rohwerder, A novel laboratory set-up for investigating surface and interface reactions during short term annealing cycles at high temperatures, Rev. Sci. Instrum. 84 (2013) 085108, https://doi.org/10.1063/1.4817310.

[30] S. Zaefferer, N.N. Elhami, Theory and application of electron channelling contrast imaging under controlled diffraction conditions, Acta Mater 75 (2014) 20–50, https://doi.org/10.1016/j.actamat.2014.04.018.

[31] W.C. Lenthe, S. Singh, M. De Graef, A spherical harmonic transform approach to the indexing of electron back-scattered diffraction patterns, Ultramicroscopy 207 (2019) 112841, https://doi.org/10.1016/j.ultramic.2019.112841.

[32] M. Takeda, T. Onishi, S. Nakakubo, S. Fujimoto, Physical properties of iron-oxide scales on Si-containing steels at high temperature, Mater. Trans. 50 (2009) 2242–2246, https://doi.org/10.2320/matertrans.M2009097.

[33] H. Siemes, B. Klingenberg, E. Rybacki, M. Naumann, W. Schäfer, E. Jansen, K. Kunze, Glide systems of hematite single crystals in deformation experiments, Ore Geol. Rev. 33 (2008) 255–279, https://doi.org/10.1016/j.oregeorev.2006.03.007.

[34] X. Zheng, S. Paul, L. Moghimi, Y. Wang, R.A. Vilá, F. Zhang, X. Gao, J. Deng, Y. Jiang, X. Xiao, C. Wu, L.C. Greenburg, Y. Yang, Y. Cui, A. Vailionis, K. Ivan, J. Llavsky, Y. Yin, C. Yi, L, Dresselhaus-Marais, correlating chemistry and mass transport in sustainable iron production, Proc. Natl. Acad. Sci. 120 (2023) e2305097120, https://doi.org/10.1073/pnas.2305097120, 1.

[35] F. Patisson, O. Mirgaux, Hydrogen ironmaking: how it works, Metals (Basel). 10 (2020) 922, https://doi.org/10.3390/met10070922.

[36] A.G. Crouch, J. Robertson, Creep and oxygen diffusion in magnetite, Acta Metall. Mater. 38 (1990) 2567–2572, https://doi.org/10.1016/0956-7151(90)90268-L.

[37] B.J. Giletti, K.C. Hess, Oxygen diffusion in magnetite, Earth Planet. Sci. Lett. 89 (1988) 115–122, https://doi.org/10.1016/0012-821X(88)90037-4.

[38] S. Yamaguchi, M. Someno, The tracer diffusivity of oxygen in wustite and cobaltous oxide, Trans. Japan Inst. Met. 23 (1982) 259–266, https://doi.org/10.2320/matertrans1960.23.259.

[39] R. Barlow, P.J. Grundy, The determination of the diffusion constants of oxygen in nickel and α-iron by an internal oxidation method, J. Mater. Sci. 4 (1969) 797–801, https://doi.org/10.1007/BF00551075.

[40] J. Takada, M. Adachi, Determination of diffusion coefficient of oxygen in α-iron from internal oxidation measurements in Fe-Si alloys, J. Mater. Sci. 21 (1986) 2133–2137, https://doi.org/10.1007/BF00547959.

[41] Y. Bai, J.R. Mianroodi, Y. Ma, A.K. da Silva, B. Svendsen, D. Raabe, Chemo-mechanical phase-field modeling of iron oxide reduction with hydrogen, Acta Mater 231 (2022) 117899, https://doi.org/10.1016/j.actamat.2022.117899.

[42] X. Zhou, Y. Bai, A.A. El-Zoka, S.H. Kim, Y. Ma, C.H. Liebscher, B. Gault, J.R. Mianroodi, G. Dehm, D. Raabe, Effect of pore formation on redox-driven phase transformation, Phys. Rev. Lett. 13 (2023) 168001, https://doi.org/10.1103/PhysRevLett.130.168001.

[43] Y. Watanabe, K. Ishii, Geometrical consideration of the crystallography of the transformation from α-Fe2O3 to Fe3O4, Phys. Status Solidi. 150 (1995) 673–686, https://doi.org/10.1002/pssa.2211500210.

[44] P. Becker, J.J. Heizmann, R. Baro, Relations topotaxiques entre des cristaux naturels d'hematite et la magnetite qui en est issue par reduetion a basse temperature, J. Appl. Crystallogr. 10 (1977) 77–78.

[45] A. Modaressi, H. El Abdouni, J.J. Heizmann, Three new orientations of the magnetite observed during the reduction of hematite between 700 and 800 °C and explanation of the multiplicity of the diff, React. Solids. 7 (1989) 19–27, https://doi.org/10.1016/0168-7336(89)80003-8.

[46] R.L. Withers, L.A. Bursill, Higher-order structural relationships between hematite and magnetite, J. Appl. Crystallogr. 13 (1980) 346–353, https://doi.org/10.1107/s0021889880012277.